

1 Diagnosing subgrid mesoscale eddy fluxes with and 2 without topography

3 **Sina Khani¹, Malte F. Jansen² and Alistair Adcroft^{1,3}**

4 ¹*Program in Atmospheric and Oceanic Sciences, Princeton University, Princeton, NJ 08540, USA*

5 ²*Department of Geophysical Sciences, University of Chicago, Chicago, IL 60637, USA*

6 ³*NOAA Geophysical Fluid Dynamics Laboratory, Princeton, NJ 08540, USA*

7 Key Points:

- 8 Subgrid mesoscale eddy fluxes and velocity scales are diagnosed as a function of
length scale using a spatial filtering approach.
- 9 In the presence of topography, subgrid scale (SGS) eddy fluxes contain a strong
standing component.
- 10 There is a strong dependence of the characteristics of SGS eddy fluxes on the di-
rection of wind stress.
- 11 • SGS eddy fluxes are modelled as a diffusion of planetary potential vorticity, and
an empirical model of diffusivity is constructed.

Corresponding author: Sina Khani (skhani@uw.edu), Current Affiliation: Applied Physics
Laboratory and School of Oceanography, University of Washington, Seattle, WA 98105,
USA

This article has been accepted for publication and undergone full peer review but has not been
through the copyediting, typesetting, pagination and proofreading process which may lead to
differences between this version and the Version of Record. Please cite this article as doi:
10.1029/2019MS001721

16 **Abstract**

17 General circulation models use subgrid-scale (SGS) parameterizations to represent the
 18 effects of unresolved mesoscale eddies on large-scale motions. Most of the current SGS
 19 parameterizations are based on a theoretical understanding of transient eddies, where
 20 the mean flow is a temporal average. Here, we use a spatial filtering analysis to better
 21 understand the scale-dependent characteristics of the SGS fluxes. Specifically, we apply
 22 the filtering approach to diagnose SGS eddy volume fluxes and eddy velocity scales in
 23 a hierarchy of model configurations from a flat-bottom channel to an idealized South-
 24 ern Hemisphere. Importantly, SGS volume fluxes include significant contributions from
 25 standing meanders; unlike for transient eddies, the vertically integrated SGS volume flux
 26 does not necessarily integrate to zero. To accommodate net vertically integrated eddy
 27 fluxes, we define a SGS eddy diffusivity based on planetary potential vorticity (PV) dif-
 28 fusion. We diagnose the transient and standing contributions to SGS fluxes and asso-
 29 ciated effective diffusivities. In the presence of bottom topography or continental bar-
 30 rriers the standing component of the PV diffusivity becomes dominant at large filter scales
 31 in the westerly wind region, while the transient component remains dominant in the east-
 32 erly wind region. Our results suggest that the diagnosed PV diffusivity can be param-
 33 eterized using mixing length theory based on *a priori* estimates of SGS velocity and length
 34 scales.

35 **1 Introduction**

36 Mesoscale eddies strongly influence the large-scale ocean circulation. These ener-
 37 getic eddies have horizontal scales of tens to a few hundred kilometers, and play a cru-
 38 cial role in the transport of heat and tracers in the ocean (e.g. Hallberg & Gnanadesikan,
 39 2006; McWilliams, 2008). Mesoscale eddies are ubiquitous but are especially prevalent
 40 near separated western boundaries and strong fronts. In the Southern Ocean, mesoscale
 41 eddies are responsible for the poleward transport of heat and equatorward transport of
 42 ocean bottom water across the Antarctic Circumpolar Current (McWilliams, 2008; Thomp-
 43 son, 2008). In numerical ocean models, a grid spacing Δ much smaller than the local Rossby
 44 radius of deformation is required to fully resolve the mesoscale eddies (Hallberg, 2013).
 45 In coarser resolution models, including many climate models, the effects of these eddies
 46 on the resolved large-scale motions have to be represented using subgrid-scale (SGS) pa-
 47 rameterizations. Ideally, such a SGS model in non-eddy permitting ocean models would
 48 be able to correctly capture eddy fluxes and their interactions with the large-scale ocean
 49 circulation.

50 Non-eddying coarse resolution ocean models generally use the Gent & McWilliams
 51 (1990, hereafter GM) parameterization to represent the extraction of available poten-
 52 tial energy (APE) from the large-scale flow via eddy volume fluxes. The GM diffusiv-
 53 ity employed for the parameterization of this process can be formulated to depend on
 54 properties of the resolved flow (e.g. Visbeck et al., 1997; Danabasoglu & Marshall, 2007).
 55 At eddy-permitting resolution, the most energetic eddies are partially resolved. Here,
 56 a resolution aware scheme seems necessary to parameterize the effects of unresolved ed-
 57 dyes. In addition to transient eddies, SGS transport can be due to unresolved standing
 58 meanders (see e.g. Treguier & McWilliams, 1990; Wolf et al., 1991; Mazloff et al., 2013),
 59 which can include a wider range of lateral scales. Therefore, SGS parameterizations may
 60 need to be resolution aware even at non-eddying resolutions in order to account for stand-
 61 ing meanders. The importance of grid spacing on parameterizations of mesoscale eddies
 62 in ocean models has long been considered in the formulation of momentum flux closures
 63 (e.g. Smagorinsky, 1963; Leith, 1996; Fox-Kemper & Menemenlis , 2008), but has only
 64 recently started to receive increasing attention in the formulation of the GM pa-
 65 rameterization (e.g. Hallberg, 2013; Bachman et al., 2017). Resolution dependence has also
 66 been studied in the context of SGS parameterizations in other types of turbulent flows
 67 in the atmosphere and ocean (e.g. atmospheric boundary layers (Porté-Agel et al., 2000);

68 buoyancy-driven turbulence (Moeng & Sullivan, 1994); stratified turbulence (Khani &
 69 Waite, 2015)), and insights from these studies can be leveraged to tackle the problem
 70 of ocean mesoscale eddy parameterization.

71 A practical approach towards developing a scale-aware SGS mesoscale eddy parameterization
 72 is to directly study the characteristics of mesoscale eddy fluxes in high resolution ocean models.
 73 Eddy fluxes in idealized high-resolution ocean models and satellite observations have been studied by Smith & Marshall (2009), Abernathey et al. (2010),
 74 Ferrari & Nikurashin (2010), and Abernathey et al. (2013), for example. In these studies,
 75 eddy fluxes are usually based on correlations of deviations from a time mean where
 76 only transient eddies are considered, or correlations of deviations from a zonal mean where
 77 the entire spectrum of standing eddies is also included. These eddy fluxes by construction
 78 assume a binary definition of the flow field into mean and eddies, and hence, can
 79 not capture the scale dependent nature of SGS fluxes. Berloff (2005) studied scale-dependent
 80 eddy fluxes for a quasi-geostrophic flow in an idealized flat bottom box. They developed
 81 a simple coarse-graining method, in which the velocity and potential vorticity (PV) from
 82 an eddy-resolving simulation are coarse-grained, and the SGS eddy fluxes are calculated
 83 by subtracting the filtered PV flux from the total flux. They applied the computed SGS
 84 eddy flux as an eddy-forcing term in a non-eddying simulation to represent the effects
 85 of mesoscale eddies (Berloff, 2005). Building on this work, Berloff (2018) employed a spatial-
 86 scale decomposition method with a filter size similar to the scale of the baroclinic ed-
 87 dies to develop a deterministic mesoscale eddy parameterization. The spatial filtering
 88 approach has also been used to diagnose the cascade of energy across scales in the ocean
 89 (Aluie et al., 2018). Related approaches are widely applied in large-eddy simulation (LES)
 90 modelling, where effective SGS momentum fluxes are measured by applying a filtering
 91 operator to the results of direct numerical simulations (see e.g. Khani & Waite, 2016,
 92 where a similar methodology is employed in stratified turbulence).

93 Following the LES approach, we here diagnose SGS mesoscale eddy fluxes as a function
 94 of scale by applying a spatial filter to the results of eddy-resolving simulations in
 95 an idealized primitive-equation ocean model. The SGS eddy fluxes are calculated by sub-
 96 tracting the fluxes computed from the product of the filtered quantities from the filtered
 97 total fluxes. Subgrid-scale eddy fluxes in this approach are filter-scale dependent and in-
 98 clude all unresolved motions, both transient and standing. This *a priori* approach [In
 99 the context of LES, an *a priori* approach refers to diagnosing subgrid scale fluxes by em-
 100 ploying an explicit filtering operator to the results of high-resolution simulations.] pro-
 101 vides important information about properties of unresolved motions, including charac-
 102 teristics of SGS eddy fluxes and the effects of eddy transport on the large-scale ocean
 103 circulation. Here, we focus on eddy volume fluxes, which are typically modelled using
 104 the GM parameterization. We apply a box filter to high resolution eddy-resolving sim-
 105 ulations in a hierarchy of models from a flat bottom channel to an idealized Southern
 106 Hemisphere configuration. Section 2 describes the model set-ups, and gives a general overview
 107 of the simulations. The Reynolds-averaged and subgrid-scale transports are described
 108 in sections 3 and 4, respectively. In Section 5, we discuss the diagnosed SGS eddy dif-
 109 fusivity and provide an interpretation in terms of a mixing-length argument. Conclu-
 110 sions are given in section 6.

112 2 Model set-up

113 We use the latest generation of the Modular Ocean Model (MOM6) code (see the
 114 GitHub repository: github.com/NOAA-GFDL/MOM6). in a strictly adiabatic config-
 115 uration, which integrates to a full equilibrium in 100 years of simulation time. The model
 116 uses six constant density layers with $\rho = 1025.5, 1027, 1027.5, 1027.8, 1028, 1028.1 \text{ [kg/m}^3\text{]}$
 117 from top to bottom, respectively. The initial layer thicknesses from top to bottom are,
 118 respectively, 150, 250, 600, 1000, 1000, 1000 [m]. The domain spans latitudes on a sphere
 119 from 65° S to 15° S and longitudes from 0° to 90° and is re-entrant in the zonal direc-

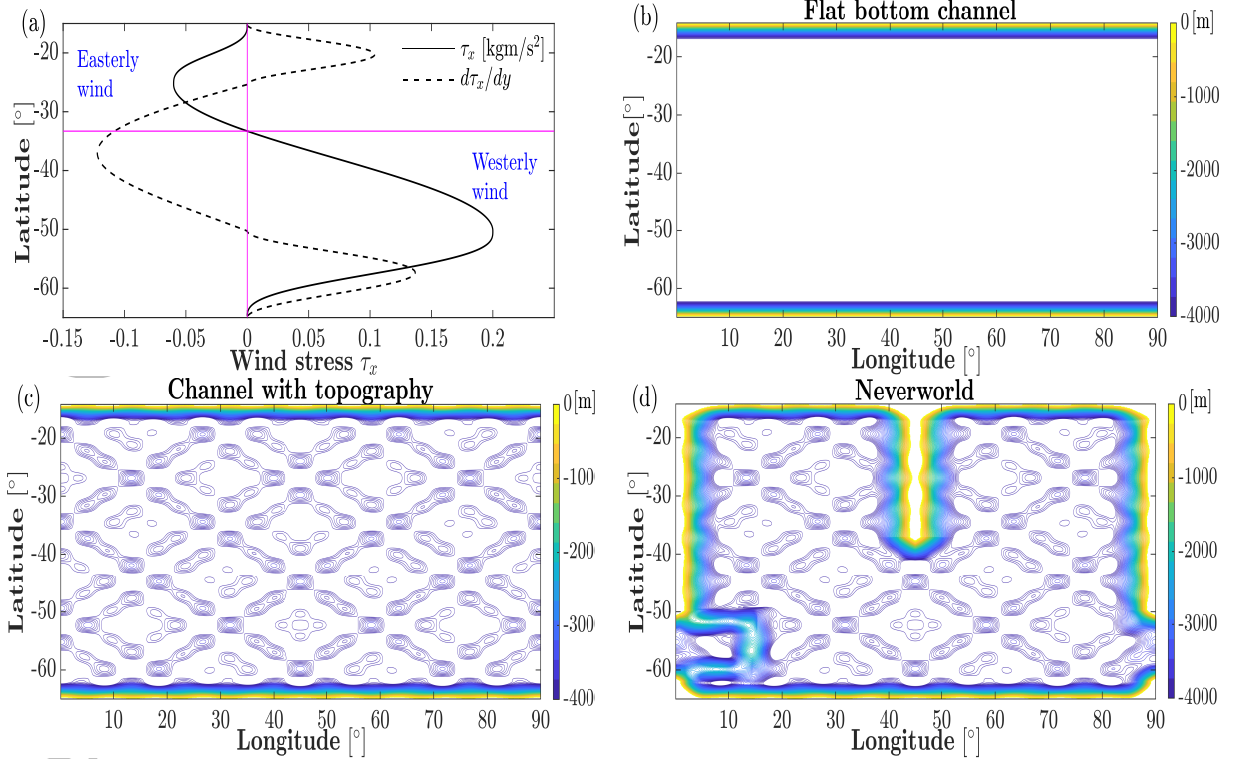


Figure 1. (a) Latitude-dependent wind stress. Ocean bathymetry in (b) flat bottom channel, (c) channel with bottom topography, (d) Southern-Hemisphere sector (Neverworld).

120 A turbulent circulation is driven by a latitude-dependent and zonally-symmetric
 121 wind stress that is distributed across the top 20 [m] of the model (figure 1a). The wind
 122 stress is easterly at low latitudes (near the equator) and westerly at mid- to high-latitudes.
 123 Three configurations for the ocean bathymetry are considered: a flat bottom channel (fig-
 124 ure 1b), a channel with bottom topography (figure 1c) and a Southern Hemisphere-like
 125 idealized continental configuration, which we call “Neverworld” (figure 1d). We have per-
 126 formed eddy-rich simulations with a horizontal resolution of $1/8^\circ$ for all configurations.
 127 An additional $1/16^\circ$ simulation was performed in the Neverworld configuration to con-
 128 firm that the results do not change significantly in finer resolution simulations. The Cori-
 129 olis parameter $f = 2\Omega \sin \theta$, where $\Omega = 7.2921 \times 10^{-5}$ [s⁻¹] and θ is the latitude in
 130 degree. Note that all domains are in the Southern Hemisphere.

131 2.1 Overview of simulations

132 All three simulations develop a turbulent flow field, illustrated via sea surface height
 133 (SSH) in figure 2 (anomaly and mean SSH are shown in the left and right panels, respec-
 134 tively). Mesoscale structures are visible in all SSH anomalies. The mean SSH shows mostly
 135 larger-scale features, although a clear imprint of bottom topography is seen in the chan-
 136 nel with topography and Neverworld simulations, particularly in the westerly wind-stress
 137 region. In channel configurations, transient mesoscale eddies are most prominent just
 138 south of the latitude where the wind direction changes sign (33°S) while the Neverworld
 139 configuration reveals strong mesoscale eddies in the Southern Ocean area and near west-
 140 ern boundaries, as well as the tip of the short continent (at 45°E), where features sim-
 141 ilar to Aghulas rings are formed.

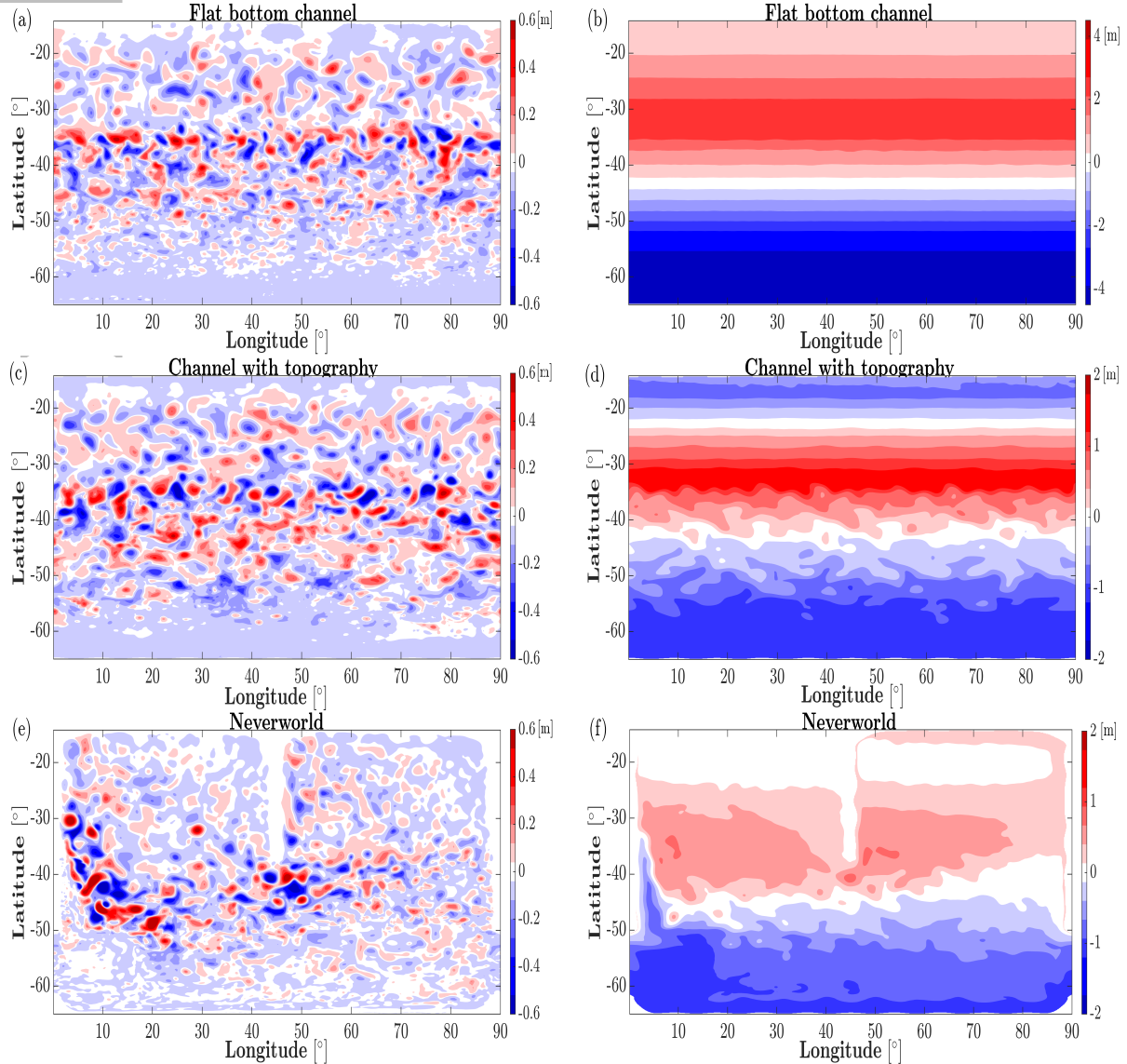


Figure 2. Sea surface height (SSH) anomaly at time $t = 75$ year (left panels) and SSH mean over the last 10 years of the simulations (right panels) for (a,b) flat bottom channel, (c,d) channel with bottom topography, and (e,f) Neverworld configurations.

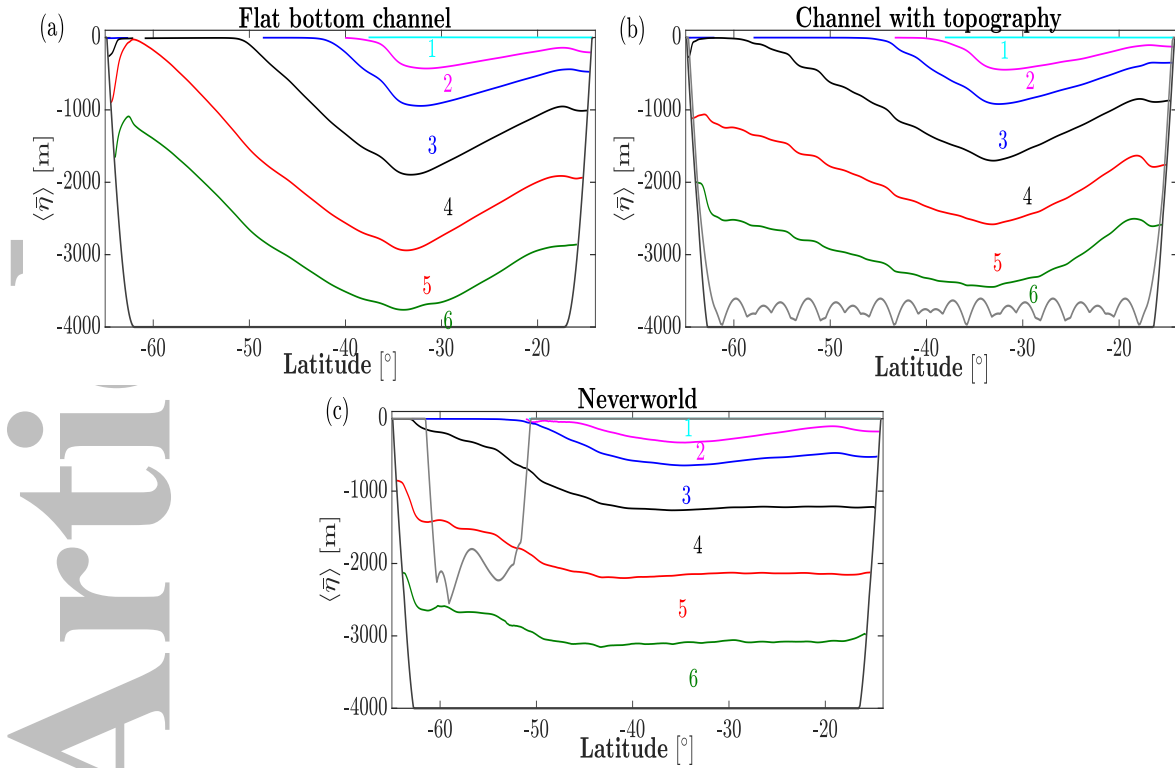


Figure 3. Time and zonally-averaged density surfaces (isopycnals) for (a) flat bottom channel, (b) channel with bottom topography, (c) Neverworld. The grey lines show the shallowest and deepest topography at the bottom of the ocean, and time averaging has been performed over the last 10 years of simulations.

142 Density surfaces (isopycnals) are tilted by the Ekman pumping (see figure 3). The
 143 sloped isopycnals indicate APE in the system, which is released via baroclinic instability.
 144 The isopycnal slopes are significantly shallower in the channel with topography com-
 145 pared to the flat bottom channel case (see panels a,b in figure 3), which is evidence for
 146 a more efficient extraction of large-scale APE when bottom topography is present (see
 147 e.g. Mazloff et al., 2013; Abernathey & Cessi, 2014). In the Neverworld configuration,
 148 isopycnal slopes in the Southern Ocean are even shallower and isopycnals in the basin
 149 region to the north are almost flat (figure 3c) – consistent with the presence of topographic
 150 barriers blocking zonal geostrophic flow.

151 Since our simulations are entirely adiabatic, no isopycnal overturning circulation
 152 can exist once a statistically steady state is reached. As a result, the meridional geostrophic
 153 transport (including mean and eddy contributions) exactly balances the wind driven cir-
 154 culation (Ekman transport), so that the time- and zonally-averaged total meridional trans-
 155 port $\langle \bar{v}h \rangle$ is exactly zero for each density layer (the bar sign $\bar{\cdot}$ and angle bracket $\langle \cdot \rangle$ de-
 156 note time and zonal averaging, respectively; v is the meridional velocity, and h is the layer
 157 thickness). In the following we will focus on the geostrophic transport, noting that the
 158 ageostrophic transport is exactly equal and opposite. The meridional geostrophic trans-
 159 port $\langle v_g h \rangle$ (where v_g representing the geostrophic velocity, calculated using the gra-
 160 dient of the Montgomery potential) is confined mostly to the top and bottom layers (fig-
 161 ure 4a), where it balances the Ekman transport. Note that layers outcrop so the top most
 162 layer changes with latitude. In the flat bottom channel, the near-surface and abyssal trans-
 163 ports balance, leading to no net meridional geostrophic transport. This balance changes

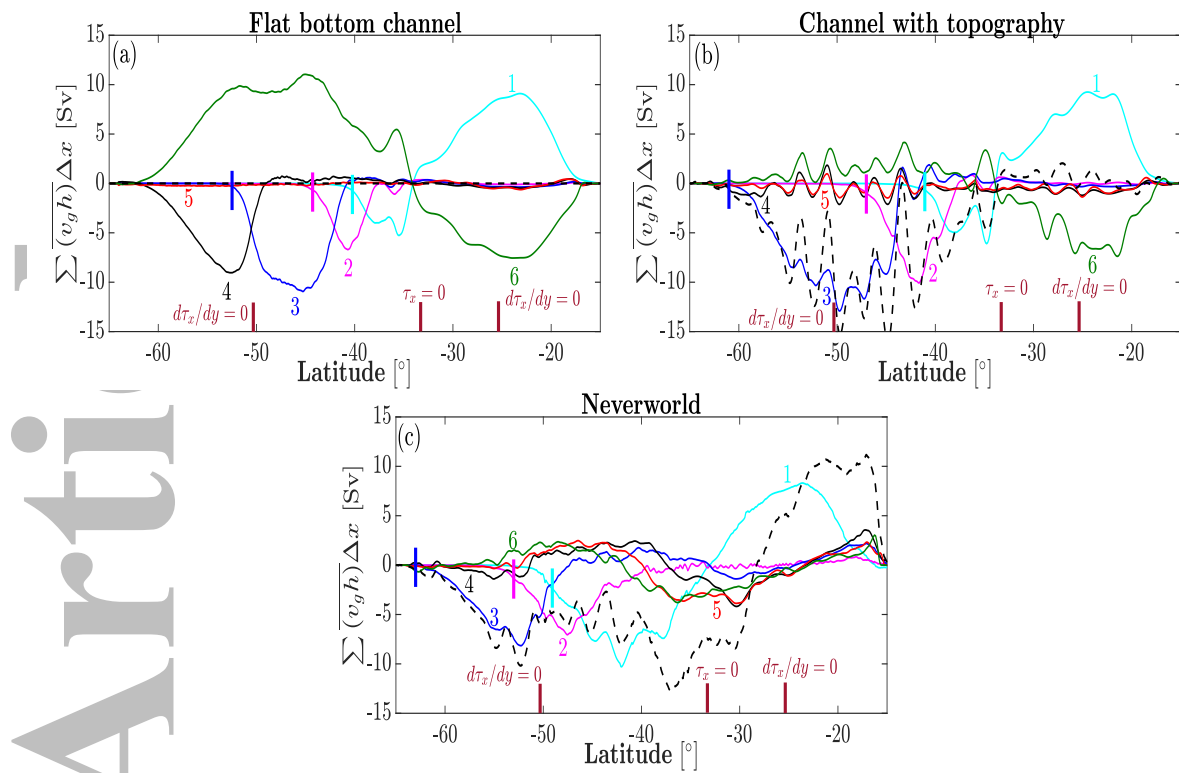


Figure 4. Time-averaged and zonally-integrated geostrophic meridional volume transport for (a) flat bottom channel, (b) channel with bottom topography and (c) Neverworld. Layers from top to the bottom are numbered from 1 to 6, respectively, the black dashed line shows the vertical sums of the geostrophic volume transports over the water column, and the small vertical lines show the location where a layer vanishes and the layer beneath is exposed to the surface. Time averaging has been performed over the last 10 years of simulations. The latitudes of zero wind and zero curl crossing are indicated. Note that $1 [\text{Sv}] = 10^6 [\text{m}^3/\text{s}]$.

in the presence of topography, where a net geostrophic transport can be maintained and related to the bottom form drag (dashed lines in figure 4, and Johnson & Bryden, 1989).

Figure 5 shows the eddy kinetic energy spectra, which are computed using the deviation from the time- and zonally-averaged velocity, at the surface in the ACC region. The energy spectra show an approximately -3 power law in the inertial sub-range, which indicates a forward enstrophy cascade below 200 [km]. For scales larger than $\sim 4^\circ$, the eddy kinetic energy spectra are flat, indicating a maximum eddy scale of around 4° .

3 Reynolds averaged transport

Existing parameterizations of eddy fluxes are motivated mostly by our physical understanding of transient eddies. Following many previous studies on eddy fluxes, we start by decomposing the time-averaged meridional geostrophic volume transport $\bar{v}_g \bar{h}$ into the mean flow and transient components using a Reynolds averaging approach

$$\bar{v}_g \bar{h} = \bar{v}_g \bar{h} + \bar{v}'_g \bar{h}', \quad (1)$$

where the prime sign denotes deviations from the time average. We will later compare these components with the SGS meridional volume transport. The time- and zonally-averaged transient $\langle \bar{v}'_g \bar{h}' \rangle$ and mean $\langle \bar{v}_g \bar{h} \rangle$ geostrophic meridional volume transports are

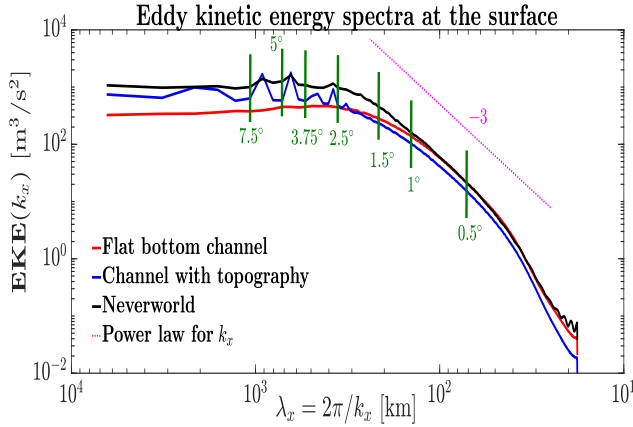


Figure 5. Time-averaged surface eddy kinetic energy spectra as a function of zonal wavelength. The spectra are averaged over the latitude 60° S to 40° S, a latitude band for the channel location in the Neverworld configuration. Time averaging has been performed over the last 10 years of simulations. The vertical lines show the Nyquist wavelengths corresponding to the horizontal filter scales, which will be discussed in section 4. Notice that all spectra are taken as a function of zonal wavenumber, but for convenience the horizontal axis has been labelled to indicate the corresponding wavelength (in km) at a latitude of $\theta = 50^\circ$ S. (At higher latitudes the same wavenumber corresponds to a somewhat smaller wavelength, while at lower latitudes it corresponds to a somewhat longer wavelength.)

shown in figure 6. In the flat bottom channel case, the wind driven circulation is balanced exclusively by transient eddies because there are no time-mean geostrophic meridional flows (figures 6a,b). In the presence of bottom topography, the time-mean transport can be non-zero and balances most of the wind driven circulation in the region with westerly wind, while the transient eddy transport remains dominant in the easterly wind region. Note that the time-mean flow component includes both contributions from the time- and zonal-mean geostrophic transport, as well as contributions from standing eddies. A further decomposition of the standing transport into an Eulerian mean overturning and standing eddy contributions is not straightforward in a stacked shallow water model, and is not attempted here.

We speculate that the qualitatively different role of the standing flow contribution in the westerly and easterly wind regions results from the difference in the PV structure and its effects on the nature of the baroclinic instability. Deeper (Phillips-type) modes, that are more influenced by bottom topography, occur in the westerly wind region, while shallower (Charney-type) modes are supported in the region with easterly wind (e.g. Tulloch et al., 2011). Moreover, the upper layers increasingly vanish in the westerly wind region, and hence there is less stratification, which is also expected to lead to deeper and less surface intensified modes. As a result, transient eddies dominantly balance the wind driven circulation in the region with easterly wind, while standing flows are dominant in the westerly wind region. The importance of topography and associated standing meanders in the region with westerly wind is consistent with the mean SSH field in figure 2, where the influence of topography structures is apparent in the westerly wind region while not seen in easterly wind region. Note that the dominance of standing meanders in the westerly region is not because the westerly wind is stronger than the easterly wind (as shown in figure 1a). We have tested this argument by reversing the wind stress sign, in which case the easterly wind becomes stronger, but standing meanders are still dominant in westerly wind region (not shown).

In the Neverworld configuration, the layer by layer volume transports are significantly more complicated than those in the channel configurations because of the continental barriers, but the transient component of the volume transports is generally much smaller than the standing component, except in the top layer of the easterly wind region (see figures 6e,f). Since there are continental barriers, the surface Ekman transport is balanced mostly by a geostrophic return transport in the interior, whose vertical integral is therefore roughly equal and opposite to the Ekman transport.

Overall, while transient eddies balance the wind-driven circulation in the flat bottom channel configuration (figure 6a,b), the time-mean geostrophic transport plays the dominant role in balancing the westerly wind stress circulation in the presence of bottom topography and/or continents (figures 6c-f). The crucial role of the time-mean geostrophic transport even in the “Drake Passage” region is at least qualitatively consistent with the results of Mazloff et al. (2013).

It is also worth noting that, since the bottom form drag has no transient contribution, the vertical integral of the time- and zonally-averaged transient geostrophic eddy fluxes is always identically zero, i.e.

$$\sum_{bot}^{top} \langle v'_g h' \rangle = 0. \quad (2)$$

This integral is shown by the black dashed lines in figure 6 for the left panels. The geostrophic mean flow transport, however, can have a non-zero depth integrated transport in the presence of bottom topography (right panels). We will return to this point in the discussion of the SGS transport in later sections.

4 Scale-dependent decomposition

We introduce a spatial filtering approach to diagnose SGS eddy fluxes in the above-mentioned models. We apply a filtering function to the high resolution eddy-rich solutions, and decompose turbulent motions into the ‘resolved’ and ‘SGS’ components with respect to the filter scale. For a variable m , we define the filtered variable as

$$\tilde{m}(i, j, t) = \sum_{i^*} \sum_{j^*} G_{\Delta_f}(i - i^*, j - j^*) m(i^*, j^*, t) A(i^*, j^*), \quad (3)$$

where $A(i, j)$ is the area of a grid-cell, G_{Δ_f} is a top-hat filtering function given as

$$G_{\Delta_f}(i - i^*, j - j^*) = \begin{cases} \frac{1}{A_{\Delta_f}}, & \text{if } |i - i^*| \leq \frac{N_f}{2} \text{ and } |j - j^*| \leq \frac{N_f}{2} \\ 0, & \text{otherwise.} \end{cases} \quad (4)$$

Here the tilde sign $\tilde{\cdot}$ denotes a filtered variable, $A(i, j)$ is the grid box area in the high resolution reference simulation and $A_{\Delta_f}(i, j)$ is the area of the filter stencil; $N_f = \Delta_f / \Delta$ where Δ_f is the filter scale and Δ is the nominal resolution of the reference simulation. Spatial filtering is not equivalent to Reynolds averaging; in particular, certain mathematical properties of Reynolds averages, such as $\bar{\bar{m}} = \bar{m}$ and $\bar{m}' = 0$, do not hold here, i.e. $\tilde{m} \neq \bar{m}$ and $\bar{m}' \neq 0$. This filtering approach is not as general as the approach for filtering on a sphere introduced by Aluie (2019). For the diagnostics of interest for the current study we do not strictly require commutation with derivatives and thus a simple filtering approach that follows the native model grid is sufficient. In Appendix A, we show unfiltered, filtered and SGS surface velocities to illustrate that how the spatial filtering operates on a field.

In the LES approach, the SGS geostrophic volume transport and kinetic energy are

$$(\mathbf{u}_g h)_{sgs} = \widetilde{\mathbf{u}_g h} - \tilde{\mathbf{u}}_g \tilde{h}, \quad (5)$$

$$\frac{1}{2} (\mathbf{u}_g^2)_{sgs} = \frac{1}{2} (\widetilde{\mathbf{u}_g \cdot \mathbf{u}_g} - \tilde{\mathbf{u}}_g \cdot \tilde{\mathbf{u}}_g), \quad (6)$$

Te

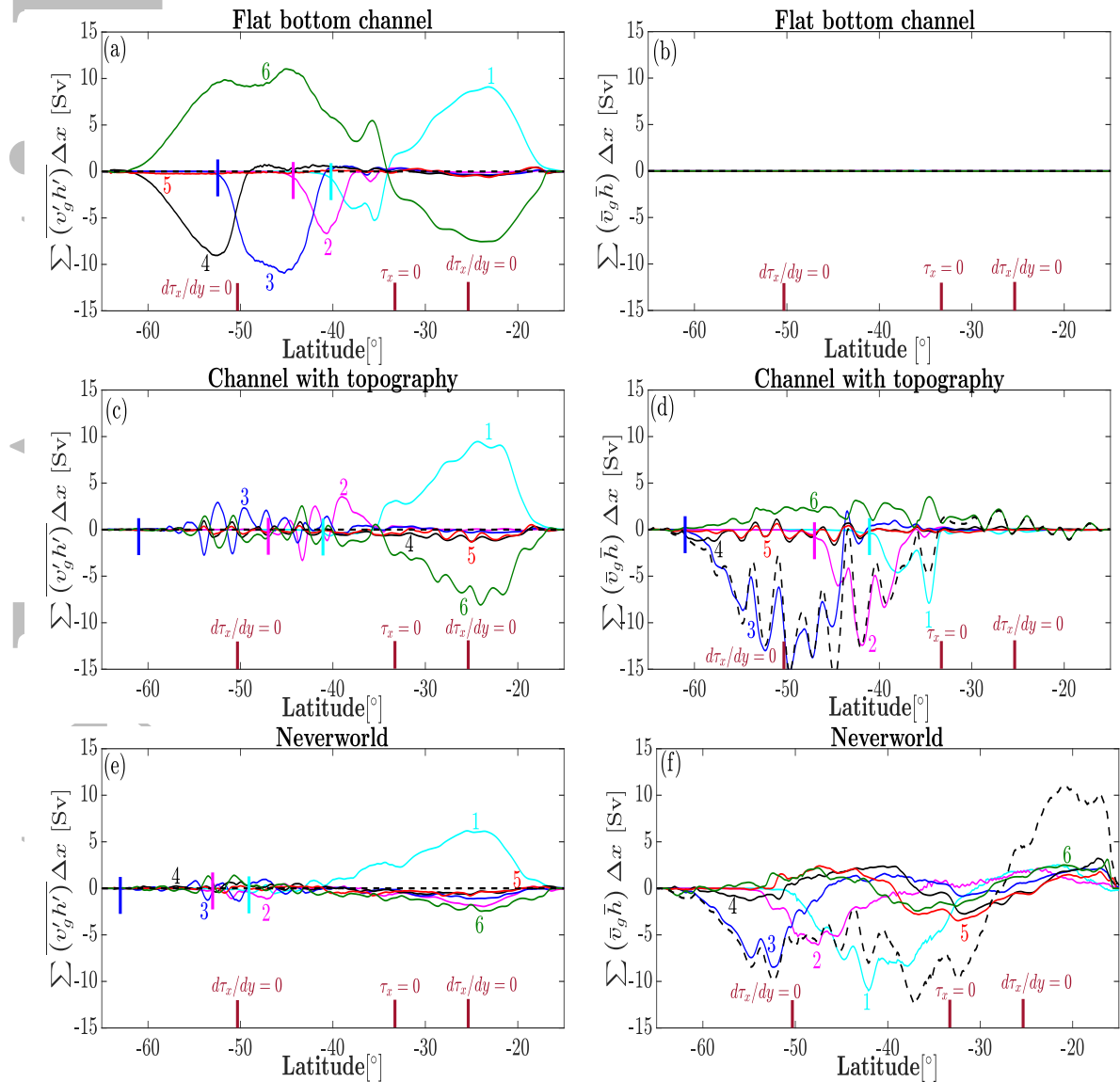


Figure 6. As figure 4, but showing the transient (left panels) and mean (right panels) components of the geostrophic meridional volume transport.

A
C
E

244 where $\mathbf{u}_g = (u_g, v_g)$ is the horizontal geostrophic velocity. We could alternatively de-
 245 fine a SGS kinetic energy as the square of the SGS velocity

$$\frac{1}{2} (\mathbf{u}_g)_{sgs}^2 = \frac{1}{2} (\mathbf{u}_g - \tilde{\mathbf{u}}_g) \cdot (\mathbf{u}_g - \tilde{\mathbf{u}}_g). \quad (7)$$

246 Although the definition in (6) is consistent with the definition of the SGS model and re-
 247 flects the missing kinetic energy in the filtered solution, equation (7) provides the kinetic
 248 energy of the SGS velocity field. The main difference between these two SGS kinetic en-
 249 ergy definitions is that the global average of SGS kinetic energy defined by equation (7)
 250 does not include the cross term between the filtered and SGS velocities, while the def-
 251 inition in (6) does (if we subtract equation (7) from equation (6) the residual is $2\tilde{\mathbf{u}}_g(\mathbf{u}_g - \tilde{\mathbf{u}}_g) +$
 252 $(\tilde{\mathbf{u}}_g^2 - \mathbf{u}_g^2)$). The first term captures correlations between the resolved and SGS veloci-
 253 ties. The second term approximately vanishes upon temporal or spatial averaging for a
 254 sufficiently homogeneous flow). In the next section, we compare these two definitions of
 255 SGS kinetic energy.

256 We can further decompose the SGS geostrophic volume transport $\overline{(\mathbf{u}_g h)_{sgs}}$ into the
 257 transient and standing components, written as

$$\overline{(\mathbf{u}_g h)_{sgs}} = \overline{(\mathbf{u}_g h)_{sgs}}^{tr} + \overline{(\mathbf{u}_g h)_{sgs}}^{st}, \quad (8)$$

258 where the transient contribution is defined as the SGS component of the transient eddy
 259 flux:

$$\overline{(\mathbf{u}_g h)_{sgs}}^{tr} \equiv \left(\widetilde{\mathbf{u}'_g h'} - \widetilde{\mathbf{u}'_g \tilde{h}'} \right) \quad (9)$$

260 and the standing component is given by the remainder of the SGS flux:

$$\overline{(\mathbf{u}_g h)_{sgs}}^{st} \equiv \overline{(\mathbf{u}_g h)_{sgs}} - \overline{(\mathbf{u}_g h)_{sgs}}^{tr} \quad (10)$$

$$= \left(\widetilde{\tilde{\mathbf{u}}_g \tilde{h}} - \widetilde{\tilde{\mathbf{u}}_g \tilde{h}} \right) + \left(\widetilde{\mathbf{u}'_g h'} + \widetilde{\mathbf{u}'_g \tilde{h}} - \widetilde{\mathbf{u}'_g \tilde{h}'} - \widetilde{\mathbf{u}'_g \tilde{h}} \right), \quad (11)$$

261 If the time averaging and filtering operators commute, the second parenthesis on the
 262 right-hand side of equation (11) vanishes. While the operators do commute in the
 263 interior, they generally do not commute near the boundaries (see 4.1 below for more in-
 264 formation). A similar decomposition can also be applied to the SGS kinetic energy.

265 We have applied the above SGS decomposition using different filter scales to the
 266 results of eddy-rich simulations, varying the filter widths across scales relevant for eddy-
 267 permitting to non-eddying ocean model resolutions. Notice that our filtering operator
 268 is unaware of the model grid (Mercator grid in our case): we average over a fixed num-
 269 ber of grid points in latitudinal and longitudinal directions. An alternative approach can
 270 be to define a filter width based on the local deformation radius (as in e.g. Berloff, 2018).
 271 This approach can provide valuable physical insights, but is less applicable to the prob-
 272 lem of eddy parameterization in non-eddying ocean models. The Nyquist wavenumbers
 273 corresponding to the selected filter scales are indicated in the eddy kinetic energy spec-
 274 tra in figure 5 (vertical green lines). The horizontal size of the largest mesoscale eddies
 275 is around 4° , where the upscale energy transfer ends (spectra become flat). We there-
 276 fore focus on the SGS volume transport with $\Delta_f = 3.75^\circ$ (the scale of the eddies) to
 277 illustrate the characteristics of SGS eddy fluxes at non-eddying resolutions. Similar re-
 278 sults are also obtained for larger filter widths.

279 We are not sure how to make a direct connection between the filtering scale and
 280 the actual grid spacing targeted by a parameterization. The numerics of ocean models
 281 generally require the solution to be smooth near the grid scale so that the effective res-
 282 olution is coarser than the grid scale. We suggest that the filter scale applied to our eddy-
 283 rich solutions be interpreted as the effective resolution of an ocean model, which might
 284 be two to four times the grid spacing but may not be well defined for non-eddying res-
 285 olutions (Soufflet et al., 2016).

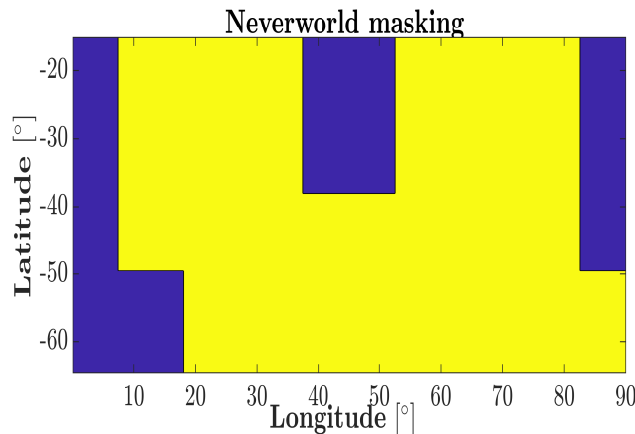


Figure 7. The Neverworld configuration mask, where the blue color shows the regions that are masked in our analysis of SGS eddy diffusivity and velocity.

286

4.1 Treatments of vanished density layers

In computing averages (be it in time or over a spatial filtering stencil) on isopycnal layers, care must be taken on how to treat isopycnal out and in-crops as well as land points (if included in the averaging domain). For the isopycnal layer thickness h , we can simply treat vanished layers as having zero thickness (consistent with the formulation of MOM6), and hence, the geostrophic thickness fluxes vanish similarly. However, to compute eddy and SGS fluxes we have to define averages of the geostrophic velocity, which is somewhat less straightforward, particularly in the presence of bottom topography.

For surface outcrops, the definition of the geostrophic velocity (based on the gradient of the Montgomery potential) can readily be extended to the vanishing part of an isopycnal, where it simply yields the surface geostrophic velocity. For isopycnal in-crops with a sloping bottom boundary, the same approach can yield spurious large geostrophic velocities even for an ocean at rest (because the layer interface overlying a vanished layer follows the topographic slope, which leads to a gradient in the Montgomery potential). We therefore treat bottom in-crops as horizontal boundaries, beyond which physical quantities are not defined.

Spatially filtered fields near boundaries are defined by reducing the size of the spatial filtering stencil to avoid land points (or in-crops). In particular, at every grid-point (i, j) , the local stencil size N_f in Eq. (4) is limited by the maximum value that ensures that no land points are included in the averaging. As a result, the shape of the filtering kernel remains unchanged but the filtering scale is reduced, such that the filtered field converges towards the full field and the SGS component vanishes near boundaries.

Since the choice of how to define filtered fields near boundaries will unavoidably affect the results, we minimize these effects when diagnosing eddy diffusivity and velocity scales in the Neverworld configuration by masking out regions around the topography (see figure 7). While this means that we are missing some of the arguably most interesting regions, we do not think that SGS fluxes can be defined unambiguously near boundaries, and hence diagnosed diffusivities would not be robust in these regions.

314 **4.2 Diagnosed SGS velocity**

315 Using the SGS kinetic energy $(1/2) (\mathbf{u}_g^2)_{sgs}$, we define the effective SGS velocity
 316 magnitude V_{sgs} as

$$V_{sgs} = \sqrt{(\mathbf{u}_g^2)_{sgs}}. \quad (12)$$

317 A second characteristic velocity magnitude is defined similarly for the alternative SGS
 318 kinetic energy definition $(1/2) (\mathbf{u}_g^2)_{sgs}^{tr}$. We, furthermore, decompose the diagnosed SGS
 319 velocity scale into the transient and standing components using the following equations

$$\overline{(\mathbf{u}_g^2)}_{sgs}^{tr} = \left(\widetilde{\mathbf{u}'_g \mathbf{u}'_g} - \widetilde{\mathbf{u}'_g} \widetilde{\mathbf{u}'_g} \right), \quad (13)$$

$$\overline{(\mathbf{u}_g^2)}_{sgs}^{st} = \overline{(\mathbf{u}_g^2)_{sgs}} - \overline{(\mathbf{u}_g^2)}_{sgs}^{tr}. \quad (14)$$

320 In order to present SGS velocities diagnosed as a function of filter scale, we separate the
 321 domain into two dynamically distinct regions (based on the easterly versus westerly wind
 322 stress) and compute area averages over each of these regions. Figure 8 shows the diag-
 323 nosed SGS velocities at the surface (local top layer) in the flat-bottom channel case based
 324 on the two definitions of SGS kinetic energy in equations (6 and 7) as a function of fil-
 325 tering scale. For comparison, we also compute a sub-scale velocity defined by integrat-
 326 ing the EKE spectrum from the corresponding Nyquist wavenumber $k_f = \pi / \Delta_f$ to the
 327 largest wavenumber. At small filter scales, the LES-based SGS velocity (as defined in
 328 equation 6) is much larger than that defined by equation (7), but the two SGS veloci-
 329 ties converge at large filter widths. When the scale of eddies is captured (i.e. $\Delta_f \gtrsim 3.75^\circ$),
 330 the diagnosed SGS velocities converge to values in between eddy and total r.m.s. veloc-
 331 ities (figure 8). This behavior demonstrates that the diagnosed SGS velocity has con-
 332 tributions of both eddy and mean velocities. The cumulative velocity from the EKE spec-
 333 trum is close to the SGS velocity scale defined based on the EKE definition in (7). For
 334 the rest of this paper, we use the LES-based definition of SGS velocity given by equa-
 335 tion (6) since this definition is consistent with the definition of SGS eddy fluxes as shown
 336 in equation (5). Notice that higher moment filtering kernels can be used to generate SGS
 337 kinetic energies that more closely reproduce the cumulative kinetic energy spectrum (Sadek
 338 and Aluie, 2018). However, the goal here is not to reproduce a spectral decomposition,
 339 but to analyze energy and flux components that cannot be represented in coarse reso-
 340 lution ocean models, and hence here we employ a simple box filter.

341 The volume-averaged SGS velocity, along with the transient and standing compo-
 342 nents, are shown in figure 9. In channel configurations, the diagnosed SGS velocities in-
 343 crease from zero when $\Delta_f \equiv \Delta$ to a value around 0.12 [m/s] with westerly wind and
 344 0.10 [m/s] with easterly wind when SGS velocities plateau around 4° (see figures 9a-d).
 345 In the Neverworld configuration, the SGS velocity converges to 0.08 [m/s] (westerly re-
 346 gion) and 0.07 [m/s] (easterly region), which is smaller than those in channel configu-
 347 rations (see figures 9e,f). This behavior shows that the SGS velocity reduces in the pres-
 348 ence of basins and/or significant topography near Drake Passage. Note that the flat bot-
 349 tom channel case naturally has no standing SGS velocity component, and the total SGS
 350 velocity is the same as its transient component. The channel with topography and Ne-
 351 verworld cases both have transient and standing SGS velocity components, for which $v_{sgs}^2 =$
 352 $v_{sgs,tr}^2 + v_{sgs,st}^2$ (subscripts ‘tr’ and ‘st’ denote the transient and standing components,
 353 respectively). Overall, the transient component of the volume-averaged SGS velocity re-
 354 mains dominant in all cases and regions, although there is a significant standing contri-
 355 bution to the SGS velocity when topography is present (figures 9c-f).

356 **4.3 SGS eddy transport**

357 In this section, we describe the SGS meridional volume transport and volume-averaged
 358 diagnosed PV diffusivity that are computed by filtering the results of the eddy-resolving
 359 simulations.

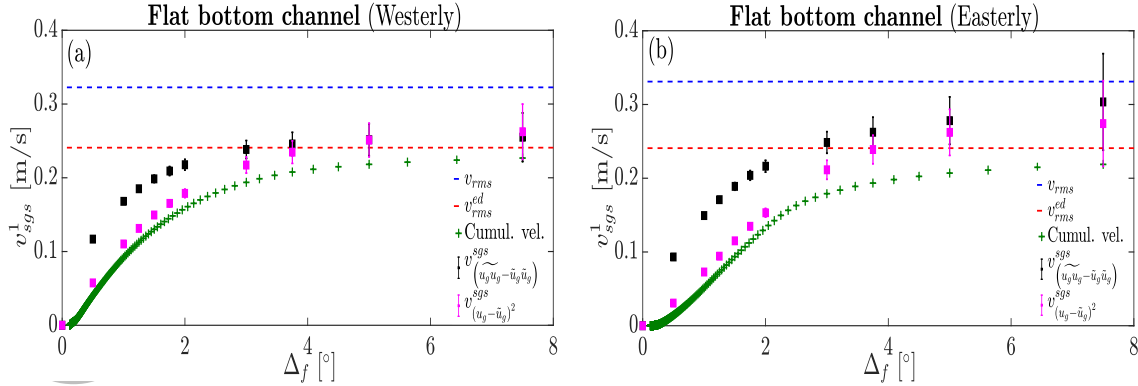


Figure 8. Area-averaged SGS velocity for the top layer $v_{sgs}^1 = \langle \overline{V_{sgs}^1} \rangle$, where $\langle \langle \cdot \rangle \rangle$ denotes a horizontal average, versus the filter width for the flat bottom channel in (a) westerly wind (latitudes $\theta < -33.3^\circ$), and (b) easterly wind (latitudes $\theta \geq -33.3^\circ$). Black and magenta squares use the SGS kinetic energy definitions in equations (6) and (7), respectively. The blue and red dashed lines show the total and eddy r.m.s. velocities (where the eddy component is defined as deviations from the time and zonal mean). Green plus signs show the cumulative spectral eddy velocity (see the text for explanation). Time averaging is performed over the last 10 years of simulations. The procedure for calculating confidence intervals is given in D1.

We start by considering the zonally integrated SGS volume transport at a filter scale of $\Delta_f = 3.75^\circ$, where most of the transient eddies are removed from the resolved flow. In this case, the SGS geostrophic meridional volume transport in the flat bottom channel (figure 10a) is very similar to the transient geostrophic meridional volume transport $\langle v' h' \rangle$ (shown in figure 6a). These similarities are because the flat bottom channel case has no mean component (figure 6b), and therefore the resolved geostrophic meridional volume transport is negligible when all eddies are encompassed by the filter when $\Delta_f \gtrsim 3.75^\circ$ (figure 10b). In the presence of bottom topography or continental barriers, the SGS geostrophic meridional volume transport is very different from the transient geostrophic volume transport in the westerly wind region, where it includes significant contributions from unresolved standing meanders, while they remain broadly similar in the easterly wind region (figures 10c,e versus figures 6c-f). Note also that, unlike for the transient eddy volume flux, the vertical integral of the SGS transport generally does not vanish in the presence of bottom topography. In the channel model, the zonally and vertically integrated SGS transport is directly related to the SGS form stress (see the discussion in Appendix B). The resolved volume transport remains relatively small in the channel with bottom topography in the region with easterly wind because the transport is dominated by transient eddies with scales smaller than the filter scale $\Delta_f = 3.75^\circ$. In the westerly wind region, the resolved meridional volume transport instead is not negligible as the standing meanders can be partially resolved (figures 10d). In the Neverworld configuration, the resolved geostrophic volume transport is generally larger than the SGS transport (figures 10e,f), showing that the large-scale geostrophic transport plays a dominant role in the presence of continental barriers.

We further decompose the SGS geostrophic meridional volume transport into transient and standing components (shown in figure 11). In the flat bottom channel, the SGS meridional volume transport again has no standing component because there are no standing meanders (see figure 6b), and the SGS transport is entirely due to transient eddies (figures 11a,b). In the channel with bottom topography, the transient SGS meridional volume transport is dominant in the easterly wind region, while the standing component is dominant with westerly wind (figures 11c,d). This behavior is in line with the Reynolds

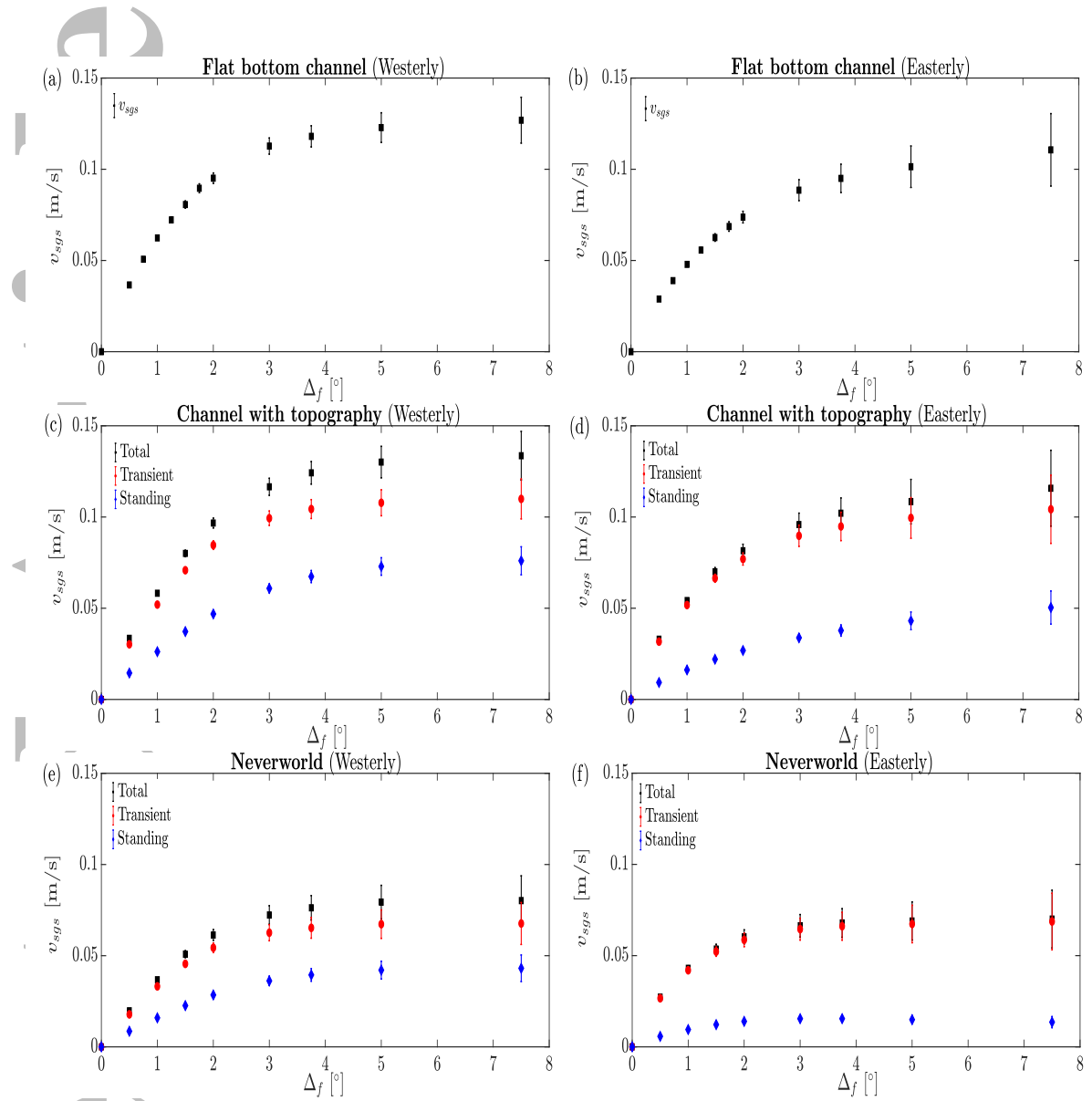


Figure 9. Diagnosed volume-weighted SGS velocity $v_{sgs} = \langle\langle\langle V_{sgs} \rangle\rangle\rangle$, where $\langle\langle\langle \cdot \rangle\rangle\rangle$ denotes a volume average, versus filter width with westerly wind (left panels) and easterly wind (right panels) for (a,b) flat bottom channel, (c,d) channel with bottom topography, and (e,f) Neverworld. Easterly and westerly winds include regions with latitudes $\theta > -33.3^{\circ}$ and $\theta < -33.3^{\circ}$, respectively, except the Neverworld configuration where the westerly region is restricted to $\theta < -50^{\circ}$ in order to isolate the dynamics in the re-entrant channel region. Time averaging is performed over the last 10 years of simulations.

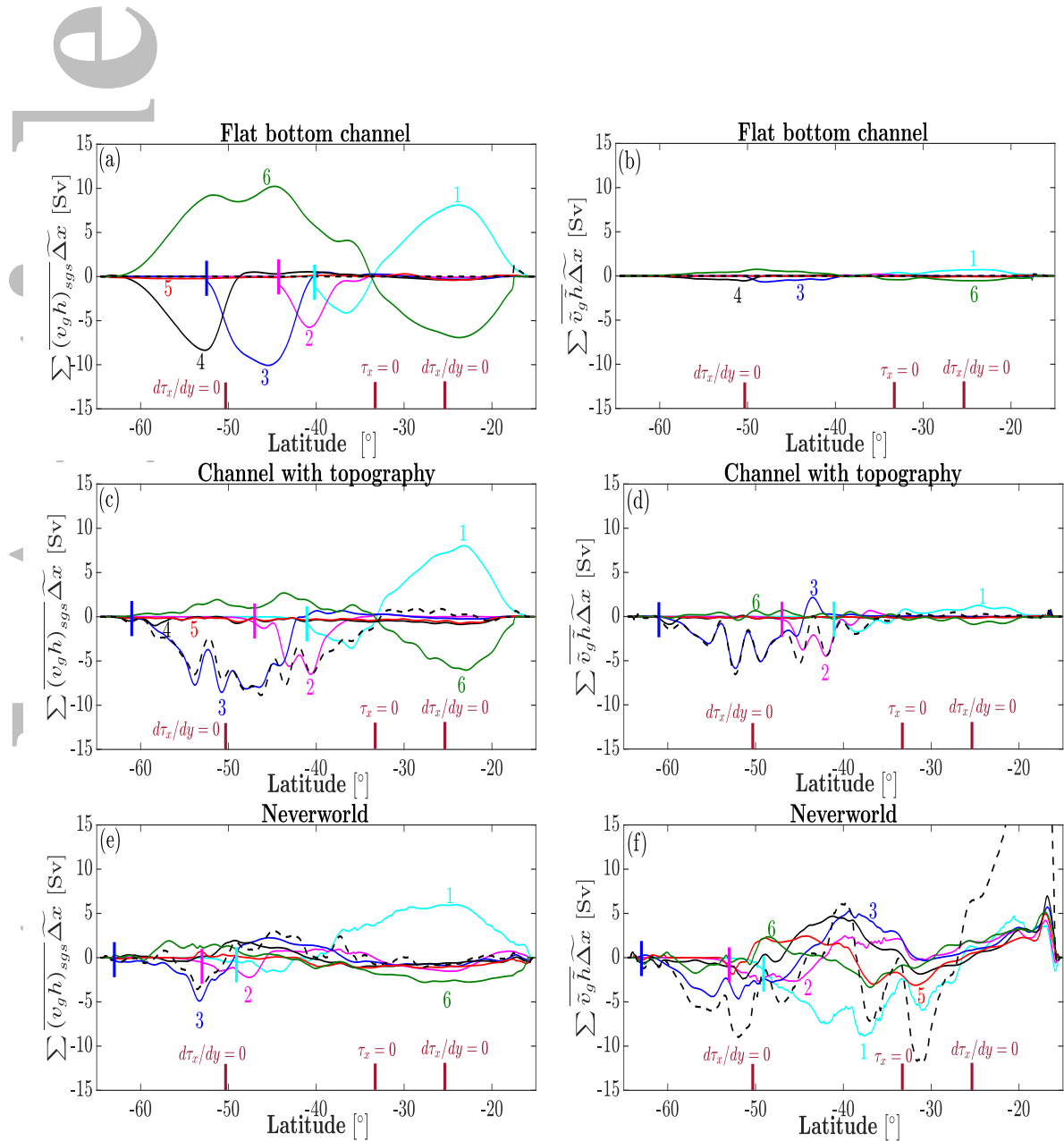


Figure 10. Time and zonally-integrated SGS (left) and resolved (right) geostrophic volume transport with the filter scale $\Delta_f = 3.75^\circ$, for (a,b) flat bottom channel, (c,d) channel with bottom topography, (e,f) Neverworld. See also the caption of figure 6.

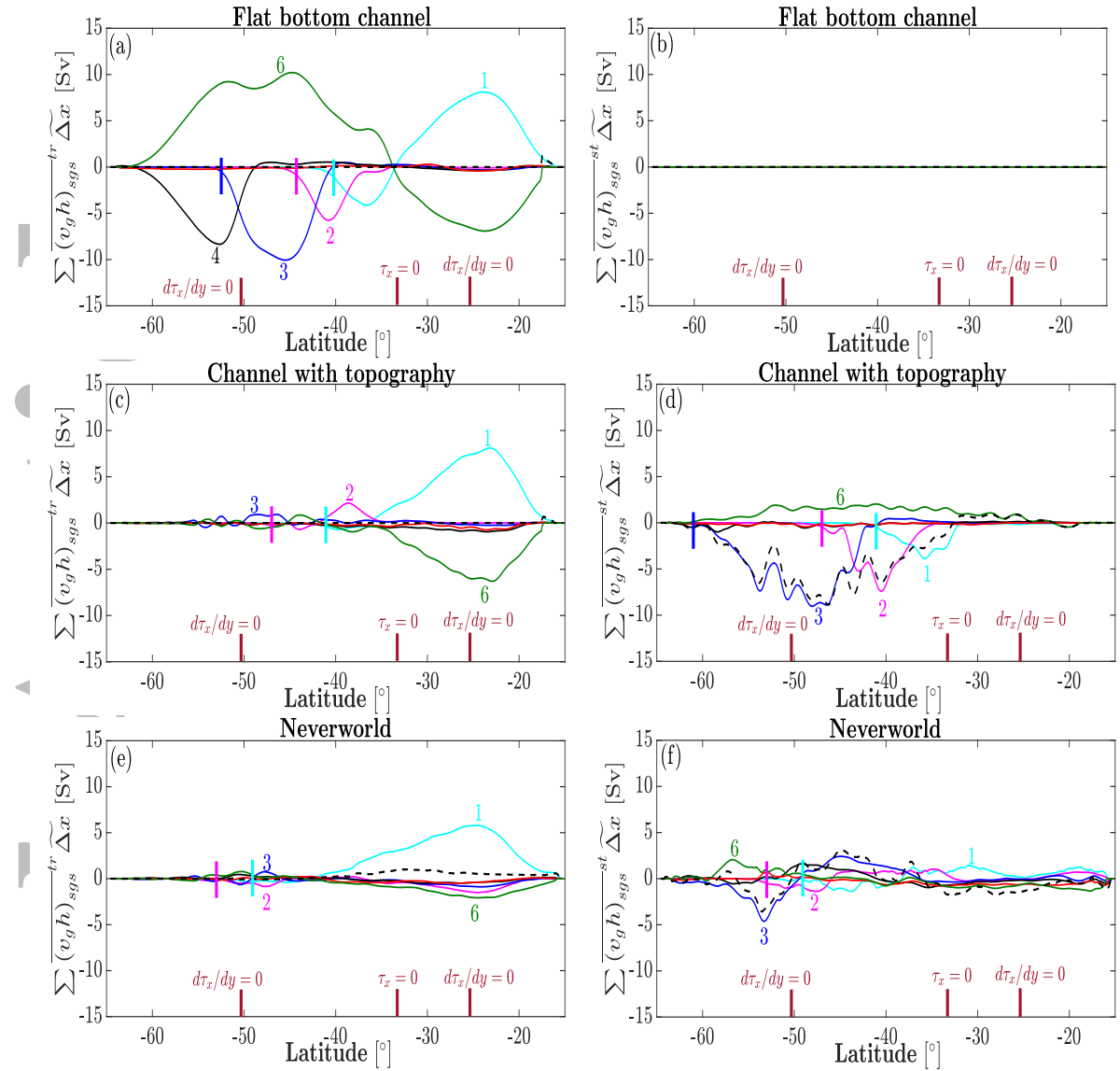


Figure 11. Time and zonally-integrated transient (left) and standing (right) SGS geostrophic volume transport with the filter scale $\Delta_f = 3.75^\circ$, for (a,b) flat bottom channel, (c,d) channel with bottom topography, (e,f) Neverworld. See also the caption of figure 6.

average decomposition, in which transient eddies and mean flow are mainly dominant in the easterly and westerly regions, respectively (see figures 6c,d). The Neverworld results are qualitatively similar to those in the channel with topography: the transient component of the SGS geostrophic volume transport is dominant in the easterly wind region, while the standing component dominates the westerly wind region (figures 11e,f). In summary, we see that the zonally-averaged SGS geostrophic volume transport is primarily due to transient eddies in all configurations where the wind is easterly. In the region with westerly wind, however, the presence of topography and/or continents results in large SGS volume transport due to unresolved standing meanders.

399 **4.3.1 Defining a “diffusivity” for eddy volume fluxes**

400 In non-eddying and eddy-permitting ocean models, we are parameterizing the SGS
 401 volume transport. In most coarse resolution ocean models, the unresolved (eddy) vol-
 402 ume transports are parameterized using the GM closure, in which the eddy volume flux
 403 is described by a stream function that is proportional to the isopycnal slope. In a stacked
 404 shallow water model the GM streamfunction is

$$\Psi_n \equiv - \sum_{k=n}^N \overline{(\mathbf{u}_g^k h^k)}_{sgs} \propto \nabla \tilde{\eta}_n, \quad (15)$$

405 where η is the isopycnal layer interface height, n indicates the isopycnal, and $N = 6$
 406 is the total number of layers. One implication of this formulation is that the vertically
 407 integrated volume transport is zero because the free surface is essentially flat (i.e. $d\tilde{\eta}_1/dy =$
 408 0) relative to interior interfaces, so that the GM model yields $\sum_1^N \overline{(v_g h)}_{sgs} \simeq 0$. This
 409 constraint may be appropriate for transient eddy fluxes, but it is not consistent with our
 410 results for the full SGS fluxes in the presence of topography and/or land (see the black
 411 dashed lines in figures 10 and 11). An important consequence of this inconsistency is that
 412 we can not unambiguously infer a GM diffusivity, as the SGS fluxes do not unambigu-
 413 ously define a streamfunction. To proceed, we here instead consider a diffusive closure
 414 for planetary PV, which is unambiguously defined. A PV diffusivity has repeatedly been
 415 suggested as a more physical closure than GM (e.g. Treguier et al., 1997; Greatbatch,
 416 1998), although we also note that a number of constraints need to be considered before
 417 it can serve as a viable prognostic closure in ocean models (see e.g. Marshall et al., 2012).
 418 Here, we compute the PV diffusivity only as a diagnostic, and we emphasize that this
 419 choice is primarily motivated because a GM diffusivity diagnostic is not unambiguously
 420 defined in our simulations.

421 As discussed in Appendix C a planetary PV flux diffusion implies a thickness flux

$$(\mathbf{u}_g h)_{sgs} = -\kappa_{pv} \nabla \tilde{h}_{pv}, \quad (16)$$

422 where κ_{pv} is the eddy PV diffusivity coefficient, and

$$\nabla \tilde{h}_{pv} = \left(\frac{d\tilde{h}}{dx}, \frac{d\tilde{h}}{dy} - \frac{\beta \tilde{h}}{\tilde{f}} \right) \quad (17)$$

423 is a modified thickness gradient. Here, β is the meridional gradient of the filtered Cori-
 424 olis parameter \tilde{f} , and we assumed that variations of f within the filtering scale are neg-
 425 ligible (see Appendix C).

426 Following equation (16), we parameterize the time- and zonally-integrated SGS geostrophic
 427 volume transport (shown in figure 10) as a function of the time- and zonally-averaged
 428 modified thickness gradient (17). Notice that the β term in the modified thickness gra-
 429 dient is relatively small, and hence qualitatively similar results to those presented be-
 430 low are obtained for a pure thickness diffusivity (c.f. Zhao & Vallis, 2008). In the absence
 431 of bottom topography, and noting that we are here solving for a vertically constant thick-
 432 ness diffusivity, the thickness diffusivity can moreover be re-interpreted as a GM diffu-
 433 sivity. In the presence of bottom topography, the relationship with the GM diffusivity,
 434 however, is not straightforward.

435 **4.3.2 Diagnosed eddy diffusivity**

436 In this section, we diagnose the effective planetary PV eddy diffusivity using a least
 437 squares method, where time and spatial averaging is performed because the local cor-
 438 relations between standing SGS eddy transport and PV gradients are very noisy. We also
 439 clip very large values of the denominator in the diffusivity calculation (which mostly hap-
 440 pens at small thickness height h near boundaries) to reduce unrealistic influence of bound-

441 ary points on the averaged eddy diffusivity. In the next section, we will model the di-
 442 agnosed eddy diffusivity via mixing length theory using the diagnosed SGS velocity as
 443 a function of filter scale.

444 Using a least squares approach, we diagnose the mean eddy diffusivities, separately
 445 for the regions of easterly and westerly winds, as (see Appendix D for more information)

$$\kappa_{pv} = -\frac{\langle\langle\langle (\mathbf{u}_g h)_{sgs} \cdot \nabla \tilde{h}_{pv} \rangle\rangle\rangle}{\langle\langle\langle \nabla \tilde{h}_{pv} \cdot \nabla \tilde{h}_{pv} \rangle\rangle\rangle}. \quad (18)$$

446 In the presence of bottom topography or continents, we also compute the transient and
 447 standing components of the planetary PV diffusivity as in (18) but using the transient
 448 and standing components of the SGS geostrophic volume transport.

449 In the easterly wind region of the channel configurations, the diagnosed diffusiv-
 450 ity increases from zero, for $\Delta_f \equiv \Delta$, up to around 600 [m²/s] at $\Delta_f \sim 4^\circ$, where the
 451 scale of the eddies is fully encompassed. Above this scale, the diffusivity plateaus (fig-
 452 ure 12b,d). The diagnosed diffusivity in the easterly wind region of the Neverworld con-
 453 figuration behaves similarly to that in the channel configurations, albeit with smaller val-
 454 ues: the diffusivity increases up to around 350 [m²/s] when the filter scale $\Delta_f = 3.75^\circ$,
 455 and plateaus around 400 [m²/s] for larger filter widths. Notice that we mask out regions
 456 near the continental boundaries in the Neverworld configuration since the filtering ap-
 457 proach becomes poorly defined at the boundaries (see 4.1). As a result we are missing
 458 some of the most energetic regions, where eddy diffusivities may be large. Overall, the
 459 diffusivities in the easterly wind regions of all configurations show qualitatively similar
 460 results, where κ_{pv} increases with the filter scale up to $\sim 4^\circ$ where it plateaus. As with
 461 the fluxes, the diffusivity is dominated by the transient component in the easterly wind
 462 region in all configurations, although the standing component in the Neverworld con-
 463 figuration increases with filter width and becomes important at large filter scales, likely
 464 due to the importance of large-scale geostrophic flows supported by lateral boundaries
 465 (see blue diamonds in figure 12f).

466 In the westerly wind region, the diagnosed eddy diffusivity shows different dynam-
 467 ics in the presence or absence of topography (or continents). In the presence of topog-
 468 raphy and land, the transient component of the diffusivity is important at small scales
 469 when $\Delta_f \lesssim 2^\circ$. However, the standing contribution becomes dominant at larger filter
 470 scales as standing meanders are not fully resolved (see figures 12c,e). In the flat bottom
 471 channel, the diagnosed PV diffusivity in the westerly wind region is similar to that with
 472 easterly wind stress since the transport is entirely due to transient eddies.

473 5 Eddy diffusivity parameterization

474 We can model an eddy diffusivity based on a velocity scale and a length scale through
 475 a mixing length argument. In this section, we try to model the planetary PV diffusiv-
 476 ity using the SGS velocity v_{sgs} , and an effective mixing length given by a function of the
 477 filter width Δ_f and an effective eddy scale L_e , written as

$$\kappa_{pv} = cv_{sgs} L_m, \quad (19)$$

478 where

$$L_m = \left(\frac{1}{\Delta_f^n} + \frac{1}{L_e^n} \right)^{-1/n}, \quad (20)$$

479 and c is a non-dimensional coefficient. The mixing length proposed in equation (20) pro-
 480 vides a length scale that is limited by the minimum of the filter and effective eddy scales
 481 Δ_f and L_e , with a smooth transition from one limiter to another. The parameter n de-
 482 termines how smooth that transition is: a smaller n gives a smoother transition, while

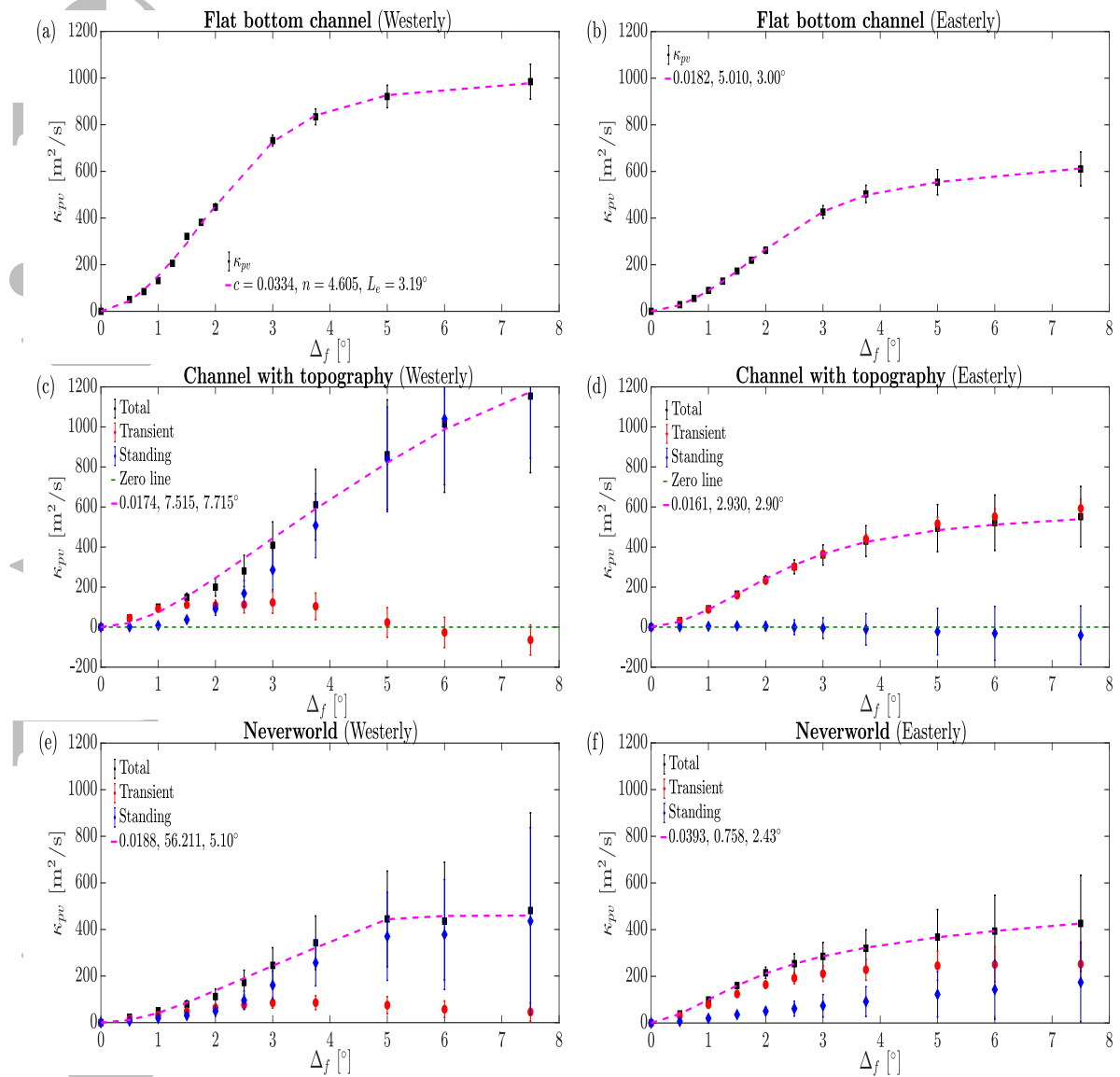


Figure 12. Diagnosed volume-averaged planetary PV diffusivity versus filter width with westerly wind (left panels) and easterly wind (right panels) for (a,b) flat bottom channel, (c,d) channel with bottom topography, and (e,f) Neverworld. Easterly and westerly winds include regions with latitudes $\theta > -33.3^\circ$ and $\theta < -33.3^\circ$, respectively (in Neverworld, however, the westerly region is restricted to $\theta < -50^\circ$ to remove the effects of continent on the filtered variables). The magenta dashed lines show the modelled diffusivity using a mixing length theory based on the SGS velocity and harmonic mean length scales, where the numbers given in the legend represent the fitted parameter values for c , n and L_e , respectively (see section 5). Time averaging is performed over the last 10 years of simulations.

483 for very large n the function simply returns the minimum of the two length scales. Us-
 484 ing the diagnosed eddy diffusivity values, we optimize parameters c , n and L_e , such that
 485 the squared errors between the modelled and diagnosed eddy diffusivities are minimized.

486 The diffusivity modelled in the form of equation (19) provides a good fit to the di-
 487 agnosed planetary PV diffusivities (Magenta dashed lines in figure 12), although the op-
 488 timized parameters (provided in the legend of figure 12) differ significantly between the
 489 different configurations and regions. In the easterly wind region, where the transient com-
 490 ponent of the PV diffusivity is dominant, the PV diffusivity parameterization agrees par-
 491 ticularly well with the diagnosed PV diffusivity. In this region, the optimized value for
 492 $L_e \approx 3^\circ$, which is close to the scale of the eddies (see figures 12b,d,f). The non-dimensional
 493 coefficient c in the easterly region is roughly similar for the two channel configurations,
 494 but it is around twice as large in the Neverworld configuration.

495 In the westerly region, where the standing component is dominant in configurations
 496 with topography and/or land, the agreement between the parameterized and diagnosed
 497 PV diffusivities is also good, but less perfect than for the easterly region (figure 12). The
 498 best fit effective eddy scale L_e in the westerly regions of the flat bottom channel is again
 499 similar to the scale of transient eddies, but it is significantly larger ($\sim 5^\circ$) in the chan-
 500 nel with topography and larger still in the Neverworld configuration ($\sim 8^\circ$). The larger
 501 maximum mixing length appears to be a result of the role of SGS standing eddies and
 502 meanders, which include a much wider range of scales (see figures 12c,e).

503 Overall, our results suggest that the eddy diffusivity parameterization based on mix-
 504 ing length theory, with the diagnosed SGS velocity and a mixing length modeled as a
 505 harmonic mean of the filter scale and a maximum “eddy” scale, is a robust approach to
 506 model the eddy diffusivity through a wide range of filter scales. That is, the diagnosed
 507 eddy diffusivity for various ocean bathymetries is predicted well by a mixing length hy-
 508 pothesis through an *a priori* study (figure 12). However, the optimized coefficients and
 509 parameters (including the non-dimensional ones) vary between model configurations and
 510 regions, suggesting that they are not universal. A more elaborate hypothesis is there-
 511 fore needed to develop a generalized parameterization. It appears that such a general-
 512 ized proposition needs to account for the role of topography and how it affects eddy trans-
 513 ports in different flow regimes (such as easterly versus westerly winds).

514 6 Conclusions

515 Subgrid-scale volume fluxes in a hierarchy of idealized eddy-resolving ocean sim-
 516 ulations are studied in this paper by introducing a spatial horizontal filtering approach.
 517 By applying different filter scales to the results of eddy-resolving simulations, we diag-
 518 nose the SGS volume transport, velocity, and effective eddy diffusivity, all as a function
 519 of scale. We show that in the presence of bottom topography or continental barriers, the
 520 SGS volume transport is strongly influenced by standing meanders.

521 In the presence of topography, we find substantial differences in the characteris-
 522 tics of eddy fluxes between regions of westerly and easterly winds; transient eddies are
 523 dominant in the easterly region while standing meanders dominate regions with west-
 524 erly wind. An important consequence of the presence of SGS standing meanders is that
 525 the vertical sum of the zonally-averaged SGS volume transport does not integrate to zero.
 526 In this case, diagnostics based on isopycnal height diffusion are not well defined. To pro-
 527 ceed, we use a planetary PV diffusivity model to parameterize SGS volume transport.
 528 In the region with easterly wind, the transient PV diffusivity increases with filter width
 529 and converges above $\Delta_f \gtrsim 4^\circ$. In the region with westerly wind, SGS transient eddies
 530 are important when $\Delta_f < 1^\circ$, while the SGS standing meanders become dominant when
 531 $\Delta_f \gtrsim 1^\circ$. We speculate that the diverging characteristics of eddy fluxes in the easterly
 532 versus westerly regions are due to different vertical mode structures: deeper modes that

533 are strongly affected by bottom topography are expected in the relatively weakly stratified
 534 westerly wind region, while shallower and surface intensified modes are expected
 535 in the easterly wind region (see e.g. Tulloch et al., 2011). Our results suggest that the
 536 wind stress direction affects SGS fluxes, and hence SGS parameterizations in general cir-
 537 culation models may need to consider these effects.

538 Moreover, we show that we can model the diagnosed SGS planetary PV diffusiv-
 539 ity using mixing length theory with the SGS velocity scale and a blend of the filter scale
 540 Δ_f and effective eddy scale L_e . The optimized eddy scale L_e is around the scale of the
 541 transient eddies in easterly regions, while the optimized L_e seems to be significantly larger
 542 due to the effect of standing meanders in westerly regions of configurations with topog-
 543 raphy and/or land. We therefore suggest that the mixing length hypothesis provides a
 544 promising route towards a diffusive closure, although a theory to predict the various model
 545 coefficients is still needed.

546 7 Acknowledgement

547 This work has benefited from comments by Steve Griffies, Hussein Aluie, David Mar-
 548 shall and an anonymous reviewer. This work was completed in part with resources pro-
 549 vided by the University of Chicago Research Computing Center (RCC). Financial sup-
 550 port was provided by National Science Foundation through award numbers 1536360 and
 551 1536450 which is gratefully acknowledged. S.K. gratefully acknowledges the hospitality
 552 of the Department of Geophysical Sciences at the University of Chicago during his visit.
 553 A.A. also acknowledges support by award NA14OAR4320106 from the National Oceanic
 554 and Atmospheric Administration, U.S. Department of Commerce. The statements, find-
 555 ings, conclusions, and recommendations are those of the author(s) and do not necessar-
 556 ily reflect the views of the National Oceanic and Atmospheric Administration, or the U.S.
 557 Department of Commerce. All source code for generating the results are available at
 558 <https://github.com/sinakhani/Neverworld>.

559 Appendix A Examples of filtered fields

560 Figure A1 shows the unfiltered, filtered and SGS fields of meridional geostrophic
 561 velocity in the surface layer for the flat bottom channel configuration when $\Delta_f = 2^\circ$.
 562 The filtered part of the meridional velocity includes mostly large-scale motions that are
 563 resolved by the filter scale $\Delta_f = 2^\circ$ while the SGS part includes small-scale structures
 564 that are below the filter width, and whose effects would therefore need to be parame-
 565 terized in coarser resolution simulations.

566 Appendix B SGS form stress

567 We can write the meridional geostrophic volume transport in the following form

$$\int_{z_b}^0 v_g dz = \int_{z_b}^0 \frac{1}{\rho_0 f} \frac{\partial p}{\partial x} dz, \quad (\text{B1})$$

568 where ρ_0 , p , f , and z are the reference density, pressure, Coriolis parameter and verti-
 569 cal direction, respectively. Variables at the bottom of the ocean are shown with subscript
 570 b , where $z_b = z_b(x, y)$ is not constant in configurations with bottom topography. Tak-
 571 ing a zonal integral over a re-entrant domain and simplifying the right-hand side of equa-
 572 tion (B1) using the Leibniz integral rule, we can write

$$\int \left(\int_{z_b}^0 v_g dz \right) dx = - \int \left(\frac{1}{\rho_0 f} p_b(x, y) \frac{\partial z_b(x, y)}{\partial x} \right) dx. \quad (\text{B2})$$

Accepted

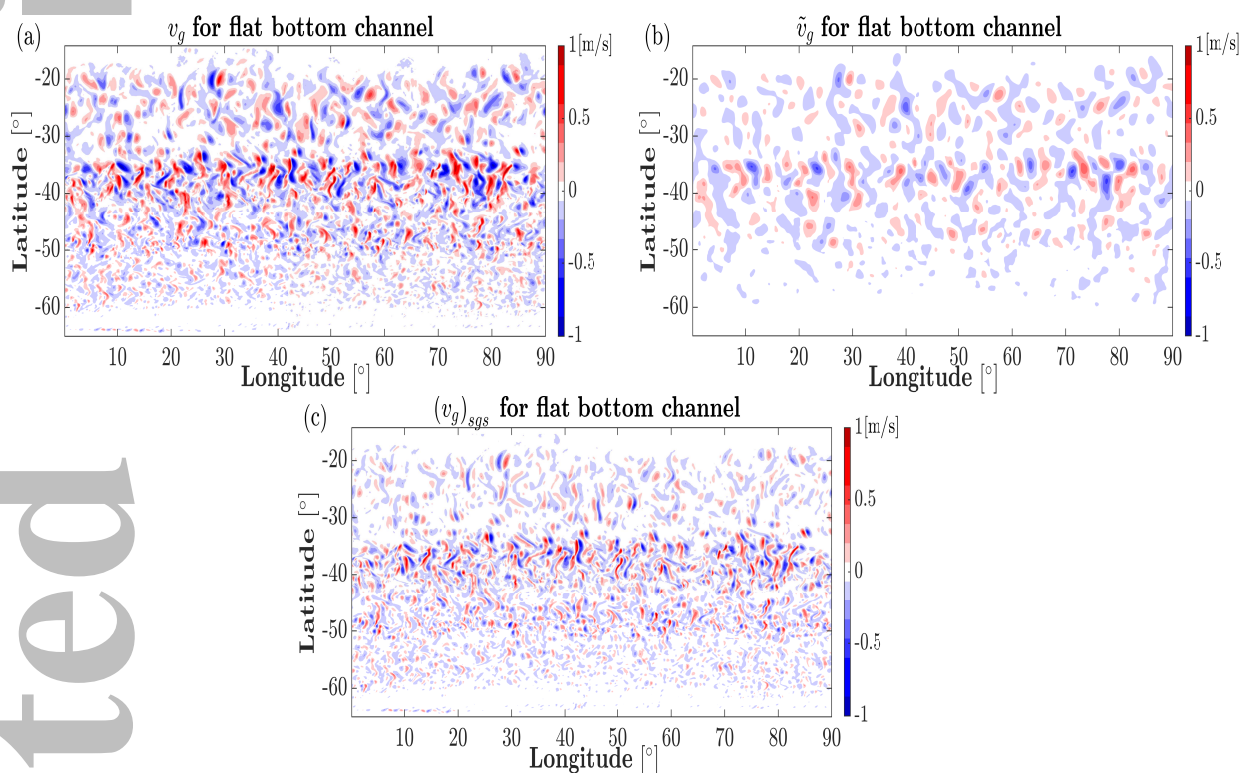


Figure A1. Meridional geostrophic velocity snapshot ($t = 75$ [yr]) at the surface layer for the flat bottom channel case: (a) unfiltered, (b) filtered and (c) SGS fields. The filter scale is $\Delta_f = 2^\circ$.

573 In stacked shallow water model, equation (B2), can be written as follows

$$\left\langle \sum_{i=1}^N v_g^i h^i \right\rangle = \frac{1}{f} \left\langle M_b \frac{\partial z_b}{\partial x} \right\rangle, \quad (\text{B3})$$

574 where $M_b = \sum_{i=1}^N g^i \eta^i$ is the Montgomery potential in the bottom model layer and the
 575 angle bracket sign $\langle \cdot \rangle$ denotes a zonal average (and we again assume a zonally re-entrant
 576 domain). By filtering equation (B3), we can get

$$\left\langle \sum_{i=1}^N \widetilde{v}_g^i \widetilde{h}^i \right\rangle = \frac{1}{f} \left\langle \widetilde{M}_b \frac{\partial \widetilde{z}_b}{\partial x} \right\rangle, \quad (\text{B4})$$

577 where we neglected contributions associated with variations in the Coriolis parameter
 578 f over the filter stencil, and we have used that the filtering operator is linear. Similarly,
 579 the zonally averaged filter-resolved meridional geostrophic transport can be written as
 580 follows

$$\left\langle \sum_{i=1}^N \widetilde{v}_g^i \tilde{h}^i \right\rangle = \frac{1}{f} \left\langle \tilde{M}_b \frac{\partial \widetilde{z}_b}{\partial x} \right\rangle, \quad (\text{B5})$$

581 where we have assumed that the filtering operator commutes with the differentiation op-
 582 erator. This commutation does not hold exactly for our filtering operator, but it is a very
 583 good approximation away from boundaries (and hence in the zonally-reentrant channel
 584 configuration).

585 If we subtract equation (B5) from (B4), we find that

$$\left\langle \sum_{i=1}^N (v_g^i h^i)_{sgs} \right\rangle = \frac{1}{f} \left\langle \left(M_b \frac{\partial z_b}{\partial x} \right)_{sgs} \right\rangle, \quad (\text{B6})$$

586 which indicates that the vertical sum of the meridional volume transport is balanced by
 587 the SGS form drag, where

$$\left(M_b \frac{\partial z_b}{\partial x} \right)_{sgs} = \widetilde{M}_b \frac{\partial \widetilde{z}_b}{\partial x} - \tilde{M}_b \frac{\partial \widetilde{z}_b}{\partial x}. \quad (\text{B7})$$

589 Appendix C Relating PV diffusion to thickness fluxes

590 We start by assuming a diffusive closure for the thickness weighted eddy PV flux:

$$(u_g q)_{sgs}^* = -\kappa_{pv} \nabla \tilde{q}^*, \quad (\text{C1})$$

591 where $q = (f + \zeta)/h$, f and ζ are the planetary and relative vorticities, respectively,
 592 $(\cdot)^* = h(\cdot)/\tilde{h}$ denotes a thickness weighted filtering, and $(u_g q)_{sgs}^* = \widetilde{u} \widetilde{q}^* - \tilde{u}^* \tilde{q}^*$ is the
 593 corresponding SGS flux. For a Reynolds averaging, a down-gradient flux closure for the
 594 thickness weighted isopycnal eddy PV flux can be motivated based on an analysis of the
 595 PV variance budget (Marshall et al., 1999; Jansen & Ferrari, 2013). Our LES filter is
 596 not a Reynolds average, and hence it is less clear in how far a diffusive closure can be
 597 justified. Nevertheless, noting the wide application of diffusive closures in GCMs, we here
 598 use it as a reasonable starting point.

599 It is a common assumption that (away from the western boundary) the gradient
 600 and flux of the relative vorticity contribution to the PV are small, such that we can ap-
 601 proximate $q \approx f/h$ (see e.g. Smith, 2007; Abernathey et al., 2010; Tulloch et al., 2011).
 602 This assumption is likely to hold well at large filter scales, although it is less clear how

well it holds at smaller scales where localized jets with significant relative vorticity can be resolved. A comprehensive treatment of volume and momentum fluxes (as suggested by e.g. Bachman et al., 2017) may be needed in this limit, but such an approach is beyond the scope of this study.

Using a planetary PV approximation, the left-hand-side of equation (C1) can be approximated as

$$(\mathbf{u}_g q)_{sgs}^* \approx \left(\frac{\widetilde{u_g f}}{\tilde{h}} \right)^* - \widetilde{u_g}^* \left(\frac{\widetilde{f}}{\tilde{h}} \right)^* = \frac{\widetilde{u_g f}}{\tilde{h}} - \frac{\widetilde{u_g h} \tilde{f}}{\tilde{h}^2}, \quad (\text{C2})$$

while the right-hand-side of equation (C1) becomes

$$-\kappa_{pv} \nabla \tilde{q}^* \approx -\kappa_{pv} \nabla \left(\frac{\widetilde{f}}{\tilde{h}} \right)^* = -\kappa_{pv} \nabla \left(\frac{\tilde{f}}{\tilde{h}} \right), \quad (\text{C3})$$

Using equations (C1-C3), we can write the meridional flux as

$$\frac{\widetilde{v_g f}}{\tilde{h}} - \frac{\widetilde{v_g h} \tilde{f}}{\tilde{h}^2} = -\kappa_{pv} \left(\frac{\beta}{\tilde{h}} - \frac{\tilde{f}}{\tilde{h}^2} \frac{d\tilde{h}}{dy} \right), \quad (\text{C4})$$

where $\beta = d\tilde{f}/dy \approx df/dy$. Substituting $\widetilde{v_g h} = \tilde{v}_g \tilde{h} + (v_g h)_{sgs}$ in equation (C4), We obtain the following equation for the SGS meridional volume transport

$$(v_g h)_{sgs} = -\kappa_{pv} \left(\frac{d\tilde{h}}{dy} - \frac{\beta \tilde{h}}{\tilde{f}} \right) + \left(\frac{\widetilde{v_g f}}{\tilde{f}} \tilde{h} - \tilde{v}_g \tilde{h} \right). \quad (\text{C5})$$

Assuming that variations of the Coriolis parameter on the scale of the filter are negligible, such that $\widetilde{v_g f} \approx \tilde{v}_g \tilde{f}$, the second parenthesis on the right-hand-side of equation (C5) is approximately zero. As a result, we can write

$$(v_g h)_{sgs} \approx -\kappa_{pv} \left(\frac{d\tilde{h}}{dy} - \frac{\beta \tilde{h}}{\tilde{f}} \right). \quad (\text{C6})$$

Similarly, we find for the SGS zonal volume transport

$$(u_g h)_{sgs} = -\kappa_{pv} \frac{d\tilde{h}}{dx}. \quad (\text{C7})$$

That is, a diffusive closure for the thickness weighted planetary PV flux leads to a thickness flux down-gradient of a modified thickness with a contribution from the planetary vorticity gradient:

$$\nabla \tilde{h}_{pv} = \left(\frac{d\tilde{h}}{dx}, \frac{d\tilde{h}}{dy} - \frac{\beta \tilde{h}}{\tilde{f}} \right). \quad (\text{C8})$$

Appendix D Least squares approach

To estimate the planetary PV diffusivity in the thickness flux equation

$$(\mathbf{u}_g h)_{sgs} = -\kappa_{pv} \nabla \tilde{h}_{pv}, \quad (\text{D1})$$

we use a least squares approach to minimize the error

$$Q = \left((u_g h)_{sgs} + \kappa_{pv} \nabla \tilde{h}_{pv} \right)^2. \quad (\text{D2})$$

Setting $\partial Q / \partial k_{pv} = 0$ yields a regression equation for the optimized PV diffusivity:

$$\kappa_{pv} = -\frac{(\mathbf{u}_g h)_{sgs} \cdot \nabla \tilde{h}_{pv}}{\nabla \tilde{h}_{pv} \cdot \nabla \tilde{h}_{pv}}. \quad (\text{D3})$$

621 **D1 Confidence interval**

622 Confidence intervals in figures 8, 9 and 12 are computed using an effective num-
 623 ber of freedom set by the filter scale. Let us assume D is found using the least squares
 624 approach for parameterizing a dependent variable \mathbf{y} in terms of an independent variable
 625 \mathbf{x} (i.e. $\mathbf{y} = \mathbf{Dx}$). We can calculate the standard error for the least square approach as
 626 follows

$$627 \text{Er} = \frac{\sqrt{\sum (y_i - Dx_i)^2 / N}}{\sqrt{\sum (x_i - \bar{x}_i)}}, \quad (\text{D4})$$

627 where \bar{x} is the mean of \mathbf{x} , and N is number of degrees of freedom. Since neighboring grid-
 628 points are generally not independent (particularly noting that the regression is applied
 629 to filtered quantities), we estimate the effective number of degrees of freedom as

$$630 N = \frac{N_{tot}}{(\Delta_f/\Delta)^2}, \quad (\text{D5})$$

631 where N_{tot} is the total number of grid points that are used in the regression, Δ_f is the
 632 filter scale, and Δ is the grid spacing of the GCM. The confidence interval provided in
 633 the figures is then computed as $D \pm z^* \text{Er}$, where we use $z^* = 1.96$ for the %95 confi-
 634 dence interval.

634 **References**

- Abernathy R. & Cessi P. 2014 Topographic enhancement of eddy efficiency in baro-
 635 clinic equilibration. *J. Phys. Oceanogr* **44**, 2107-2126.
- Abernathy R., Marshall J., Mazloff M. & Shuckburgh E. 2010 Enhance-
 636 ment of mesoscale eddy stirring at steering levels in the Southern Ocean.
J. Phys. Oceanogr **40**, 170-184.
- Abernathy R., Ferreira D. & Klocker A. 2013 Diagnostics of isopycnal mixing in a
 637 circumpolar channel. *Ocean Modelling* **72**, 1-16.
- Aluie H. 2019 Convolutions on the sphere: commutation with differential operators.
Int. J. Geomath. **10 : 9**, <https://doi.org/10.1007/s13137-019-0123-9>.
- Aluie H., Hecht M. & Vallis G. K. 2018 Mapping the energy cascade in the North
 644 Atlantic Ocean: the coarse-graining approach. *J. Phys. Oceanogr* **48**, 225-244.
- Bachman S. D., Fox-Kemper B. & Pearson B. 2017 A scale-aware subgrid model for
 645 quasi-geostrophic turbulence. *J. Geophys. Res. Oceans* **122**, 1529-1554.
- Berloff P. S. 2018 Dynamically consistent parameterization of mesoscale eddies. Part
 646 III: Deterministic approach. *Ocean Modelling* **127**, 1-15.
- Berloff P. S. 2005 On dynamically consistent eddy fluxes. *Dyn. Atmos. Oceans* **38**,
 647 123-146.
- Danabasoglu G. & Marshall J. 2007 Effects of vertical variations of thickness diffu-
 652 sivity in an ocean general circulation model. *Ocean Modelling* **18**, 122-141.
- Fox-Kemper B. & Menemenlis D. 2008 Can large eddy simulation techniques im-
 653 prove mesoscale rich ocean models? *Ocean Modeling in an Eddying Regime* M.
 654 W. Hecht and H. Hasumi eds. *Geophys. Monogr. Ser.* **177**, 319-337.
- Ferrari R. & Nikurashin M. 2010 Suppression of eddy diffusivity across jets in the
 655 Southern Ocean. *J. Phys. Oceanogr* **40**, 1510-1519.
- Gent P. R. & McWilliams J. C. 1990 Isopycnal mixing in ocean circulation model.
 656 *J. Phys. Oceanogr* **20**, 150-155.
- Greatbatch R. J. 1998 Exploring the relationship between eddy-induced transport
 657 velocity, vertical momentum transfer, and the isopycnal flux of potential vorticity.
J. Phys. Oceanogr **28**, 422-432.
- Hallberg, R. 2013 Using a resolution function to regulate parameterizations of
 658 oceanic mesoscale eddy effects. *Ocean Modelling* **72**, 92-103.

- Hallberg, R., Gnanadesikan, A. 2006 The role of eddies in determining the structure and response of the wind-driven Southern hemisphere overturning: results from the modeling eddies in the Southern ocean (MESO) project. *J. Phys. Oceanogr.* **36**, 2232-2252.
- Jansen M. and Ferrari R. 2013 The vertical structure of the eddy diffusivity and the equilibration of the extratropical atmosphere. *J. Atmos. Sci.*, **70**(5), 1456-1469.
- Jansen M. F. & Held I. M. 2014 Parameterizing subgrid-scale eddy effects using energetically consistent backscatter. *Ocean Modelling* **80**, 36-48.
- Jansen M. F., Held I. M., Adcroft A. & Hallberg R. 2015 Energy budget-based backscatter in an eddy permitting primitive equation model. *Ocean Modelling* **94**, 15-26.
- Johnson, G. C. & Bryden, H. L. 1989 On the size of the Antarctic Circumpolar Current. *Deep Sea Research Part A. Oceanographic Research Papers* **36**(1), 39-53.
- Khani S. & Waite M. L. 2013 Backscatter in stratified turbulence. *Eur. J. Mech. B/Fluids* **60**, 1-12.
- Khani, S. & Waite, M. L. 2015 Large eddy simulations of stratified turbulence: the dynamic Smagorinsky model. *J. Fluid Mech.* **773**, 327-344.
- Leith C.E. 1996 Stochastic models of chaotic systems *Physica D: Nonlinear Phenomena* **98** 481-491.
- Marshall D. P., Maddison J. R. & Berloff P. S. 2012 A framework for parameterizing eddy potential vorticity fluxes. *J. Phys. Oceanogr* **42**, 539-557.
- Marshall D. P., Williams R. G. & Lee M.-M. 1999 The relation between eddy-induced transport and isopycnal gradients of potential vorticity. *J. Phys. Oceanogr* **29**, 1571-1578.
- Mazloff M. R., Ferrari R. & Schneirder T. 2013 The force balance of the Southern Ocean meridional overturning circulation. *J. Phys. Oceanogr* **43**, 1193-1208.
- McWilliams J. C. 2008 The nature and consequence of oceanic eddies. *Geophysical Monograph Series* **177**, American Geophysical Union, Washington, D. C.
- Moeng C.-H. & Sullivan P. P. 1994 A comparison of shear- and buoyancy-driven planetary boundary layer flows. *J. Atmos. Sci.* **51**(7), 992-1022.
- Porté-Agel F., Meneveau C. & Parlange M. 2000 A scale-dependent dynamic model for large-eddy simulation: application to a neutral atmospheric boundary layer. *J. Fluid Mech.* **415**, 261-284.
- Sadek M. & Aluie H. 2018 Extracting the spectrum of a flow by spatial filtering. *Phy. Rev. Fluids* **3**, 124610.
- Smith K. S. & Marshall J. 2009 Evidence for enhanced eddy mixing at middepth in the Southern Ocean. *J. Phys. Oceanogr* **39**, 50-69.
- Smith K. S. 2007 The geography of linear baroclinic instability in Earth's oceans. *J. Mar. Res.* **39**(5), 655-683.
- Smagorinsky J. 1963 General circulation experiments with the primitive equations. *Mon. Wea. Rev.* **91**, 99-164.
- Soufflet Y., Marchesiello P., Lemarié F., Jouanno J. & Co-workers 2016 On effective resolution in ocean models. *Ocean Modelling* **98**, 36-50.
- Thompson A. F. 2008 The atmospheric ocean: eddies and jets in the Antarctic Circumpolar Current. *Phil. Trans. R. Soc. A* **366**, 4529-541.
- Treguier A. M. & McWilliams J. C. 1990 Topographic influences on wind-driven, stratified flow in a β -plane channel: an idealized model for the Antarctic Circumpolar Current. *J. Phys. Oceanogr* **20**, 321-343.
- Tulloch R., Marshall J., Hill C. & Smith K. S. 2011 Scales, growth rates, and spectral fluxes of baroclinic instability in the ocean. *J. Phys. Oceanogr* **41**, 1057-1076.
- Treguier A. M., Held I. & Larichev V. D. 1997 Parameterization of quasigeostrophic eddies in primitive equation ocean model. *J. Phys. Oceanogr* **27**, 567-580.

- 718 Visbeck M., Marshall J., Haine T. & Spall M. 1997 Specification of eddy transfer
719 coefficients in coarse-resolution ocean circulation models. *J. Phys. Oceanogr.* **27**,
720 381-402.
- 721 Wolff J.-O., Maier-Reimer E. & Olbers D. J. 1991 Wind-driven flow over topography
722 in a zonal β -plane channel: a quasi-geostrophic model of the Antarctic Circumpolar
723 Current. *J. Phys. Oceanogr* **21**, 236-264.
- 724 Zhao R. & Vallis G. 2008 Parameterizing mesoscale eddies with residual and Eulerian
725 schemes, and a comparison with eddy-permitting models. *Ocean Modelling*
726 **23**, 1-12.

Accepted Article

Figure 1.

Accepted Article

Article

Accepted

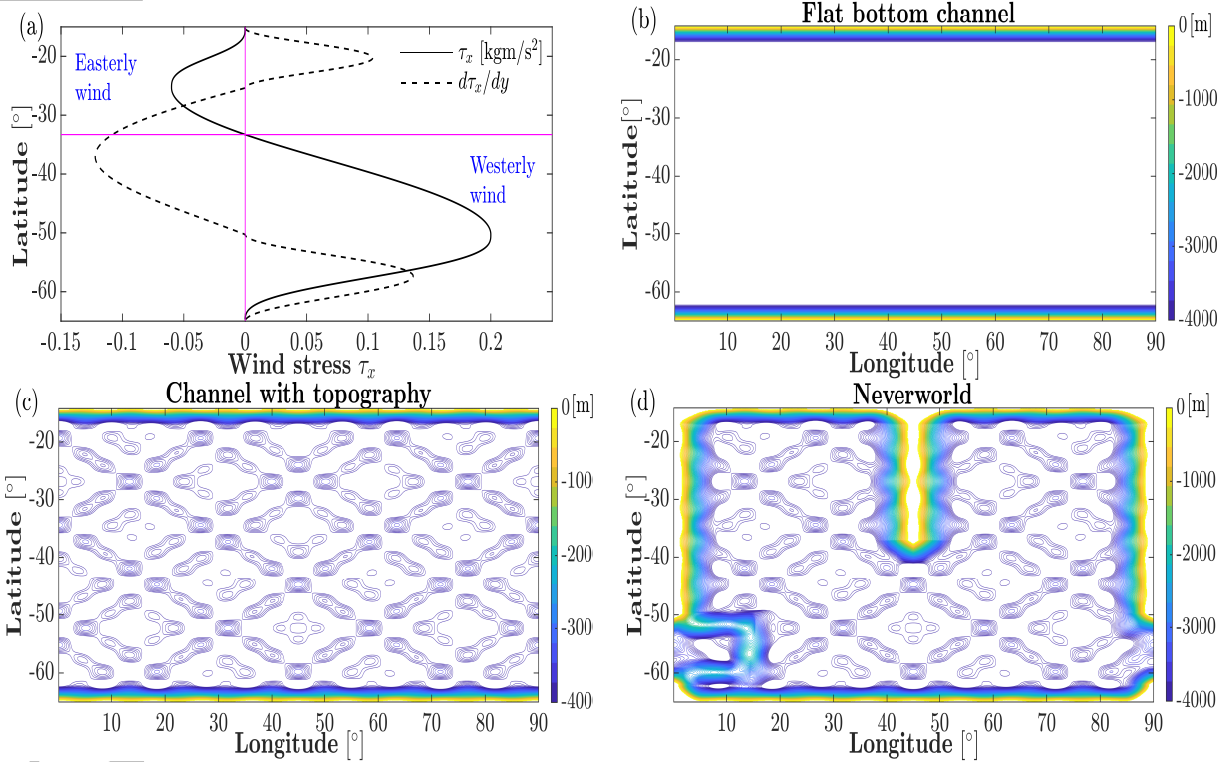


Figure 2.

Accepted Article

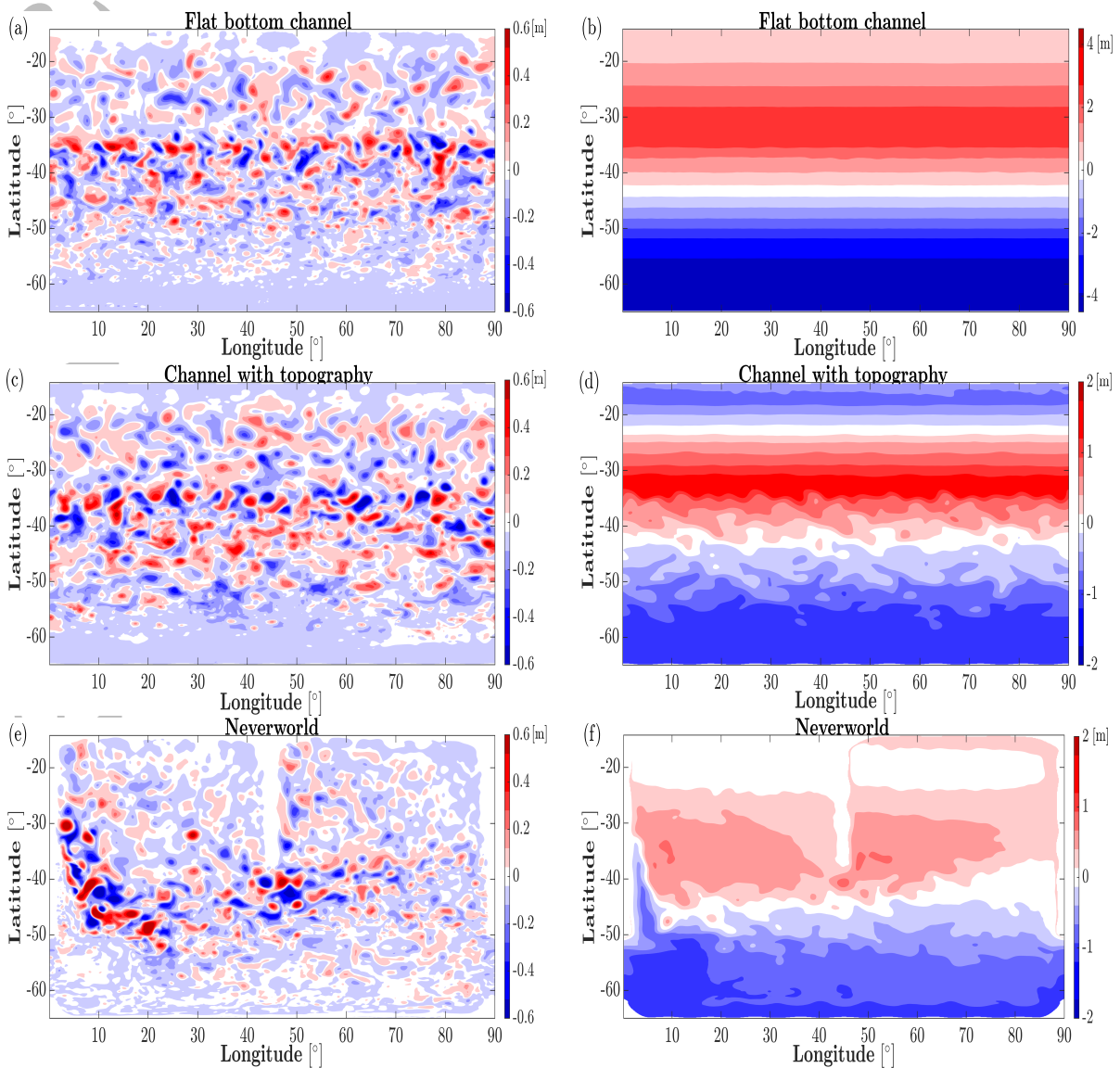


Figure 3.

Accepted Article

Accepted Article

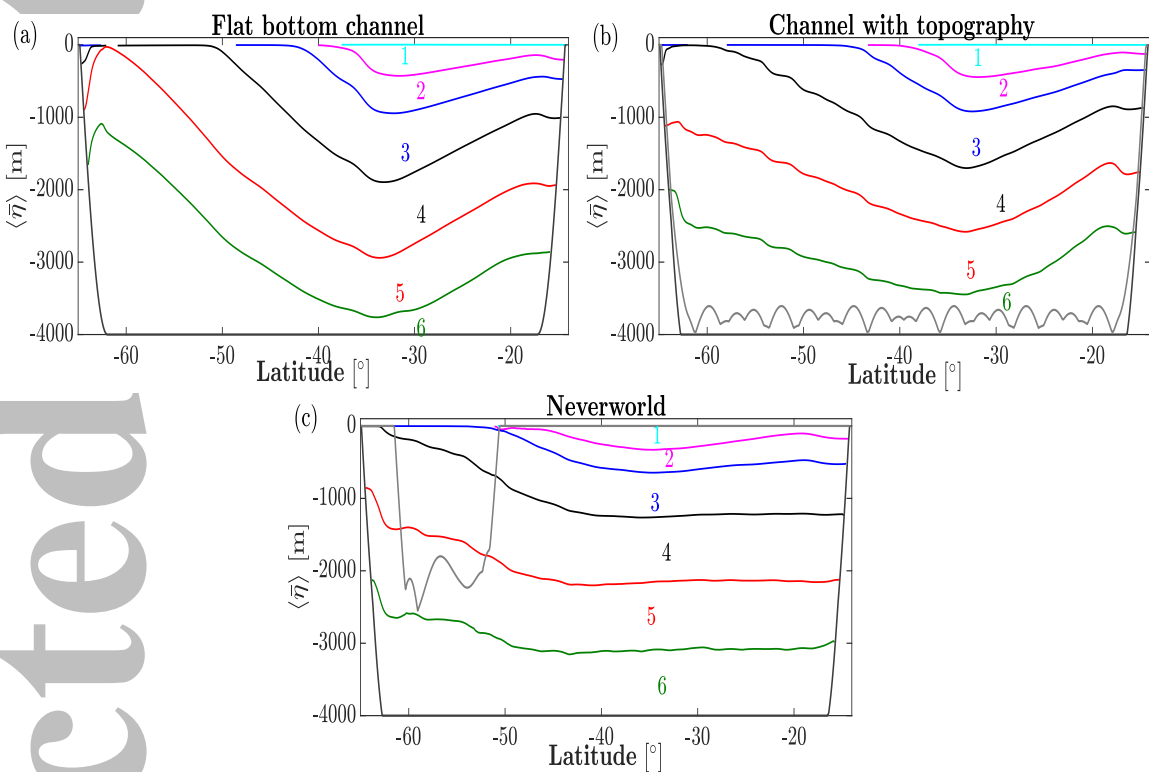


Figure 4.

Accepted Article

Accepted Article

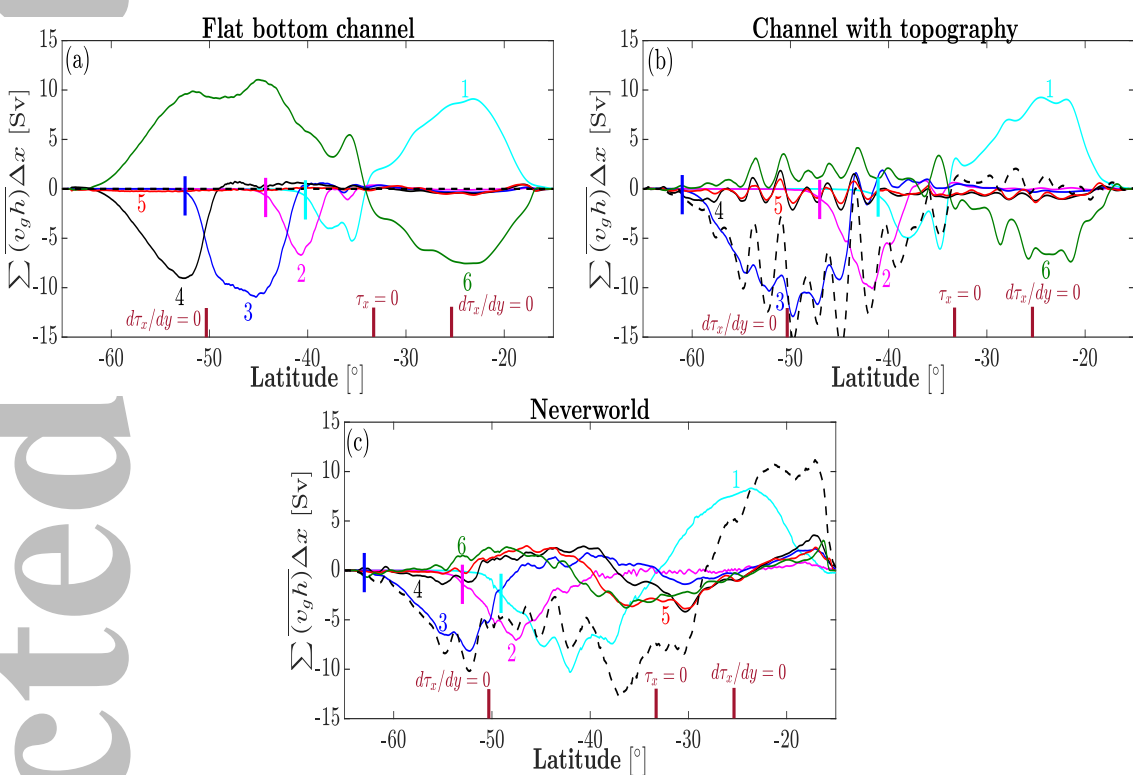


Figure 5.

Accepted Article

Accepted Article

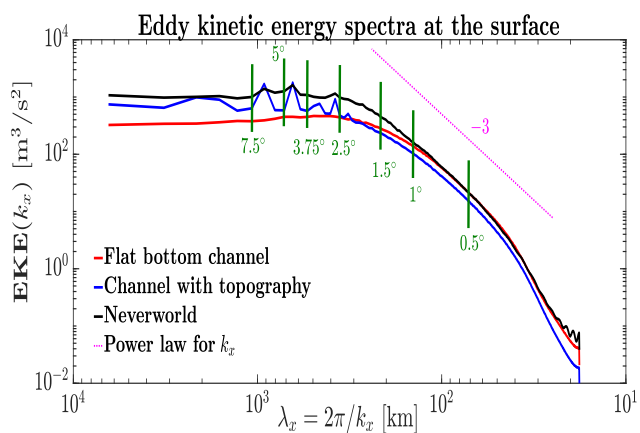


Figure 6.

Accepted Article

Jie
ACC

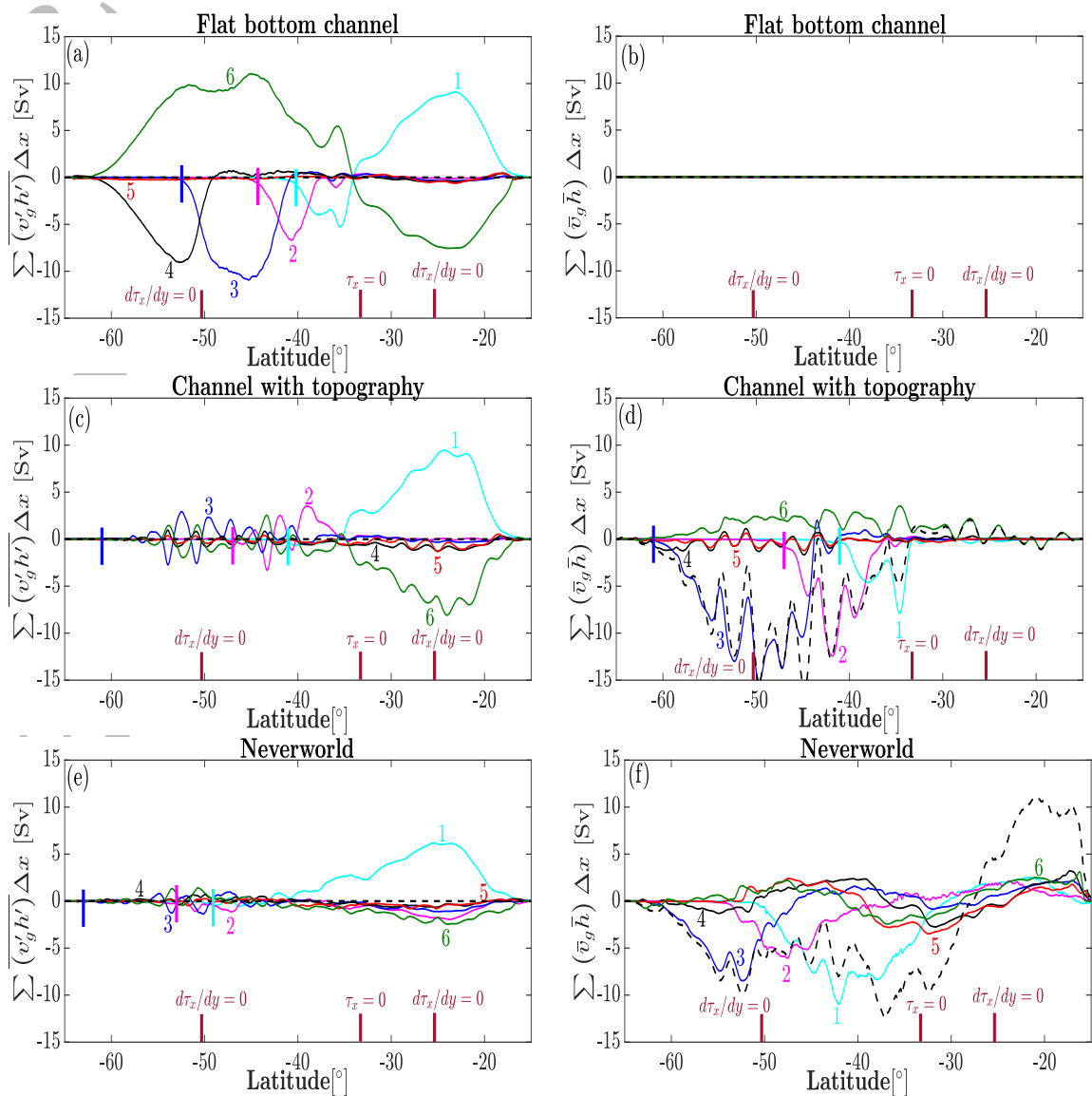


Figure 7.

Accepted Article

Accepted Article

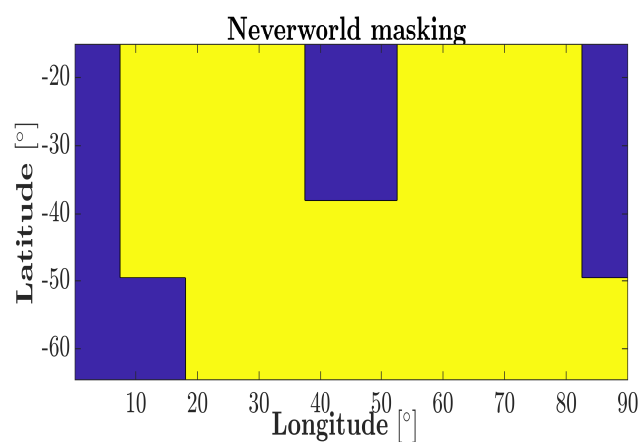


Figure 8.

Accepted Article

Accepted Article

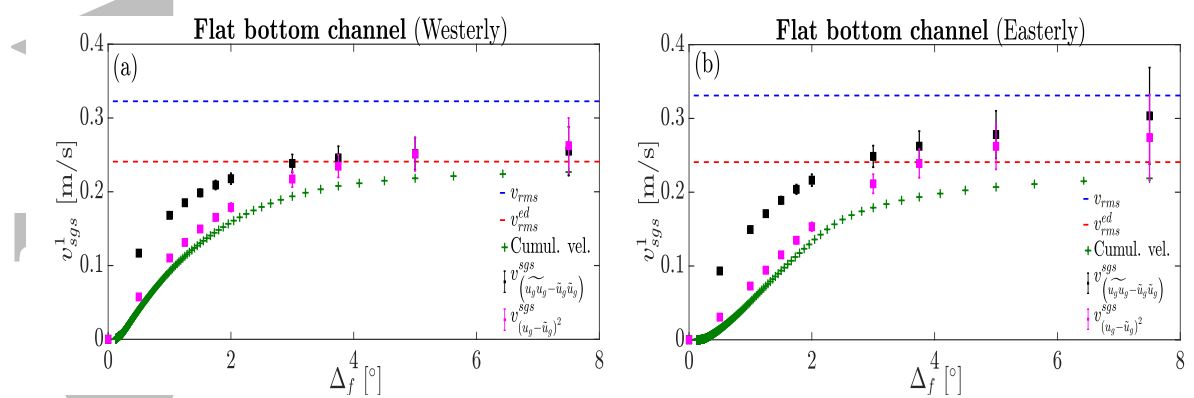


Figure 9.

Accepted Article

J
e
A
C
C

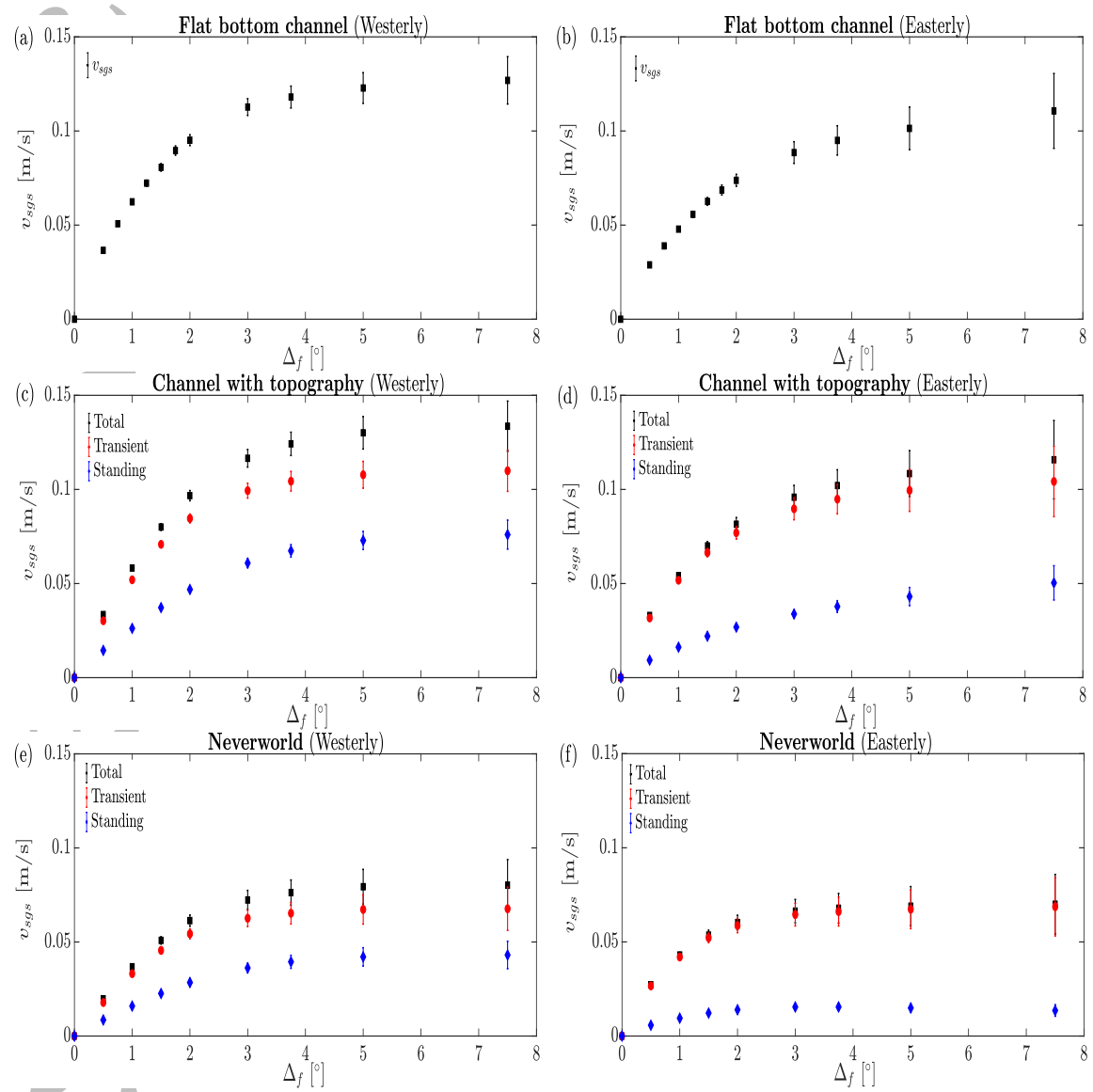


Figure 10.

Accepted Article

Jie
ACC

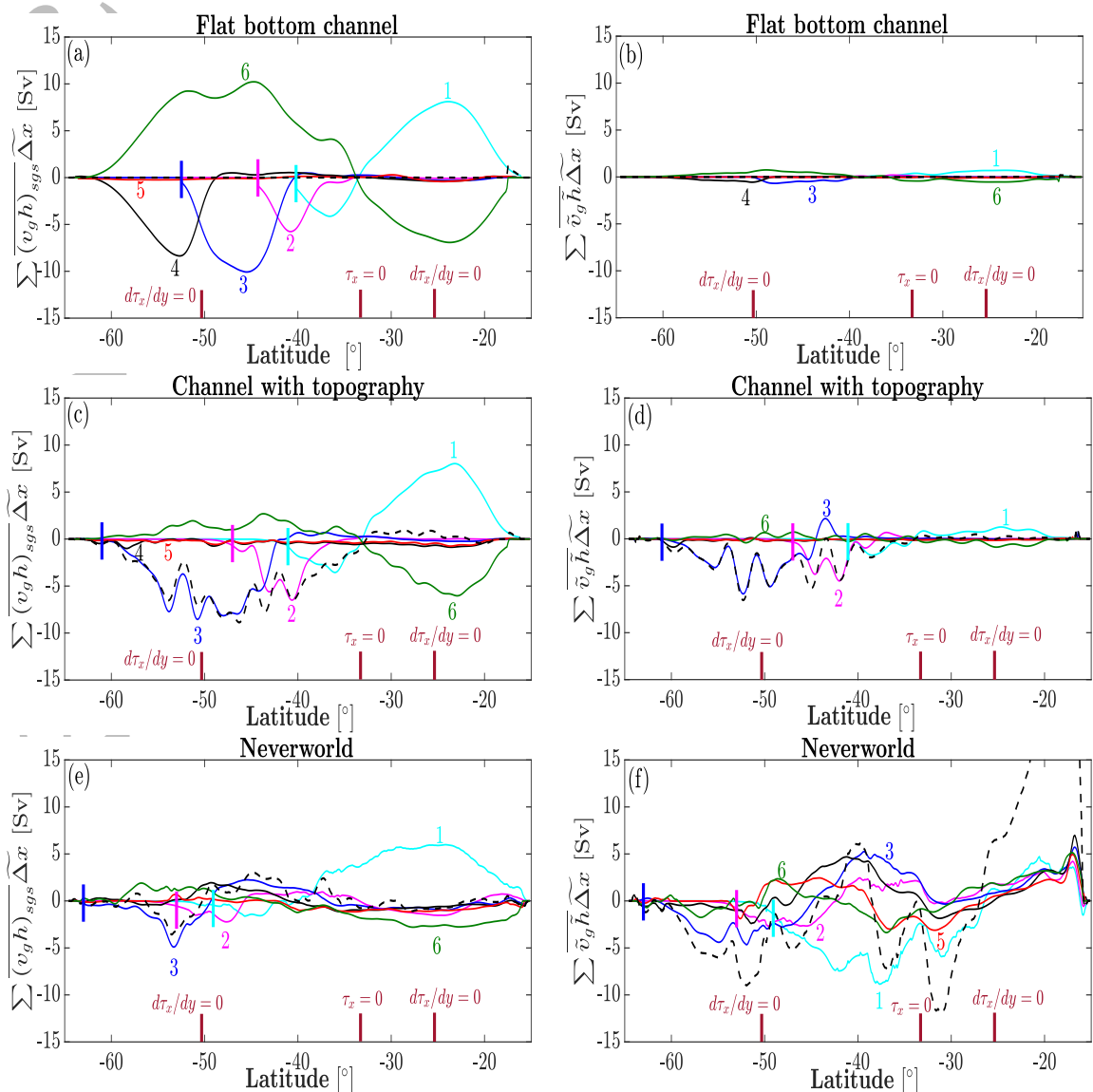


Figure 11.

Accepted Article

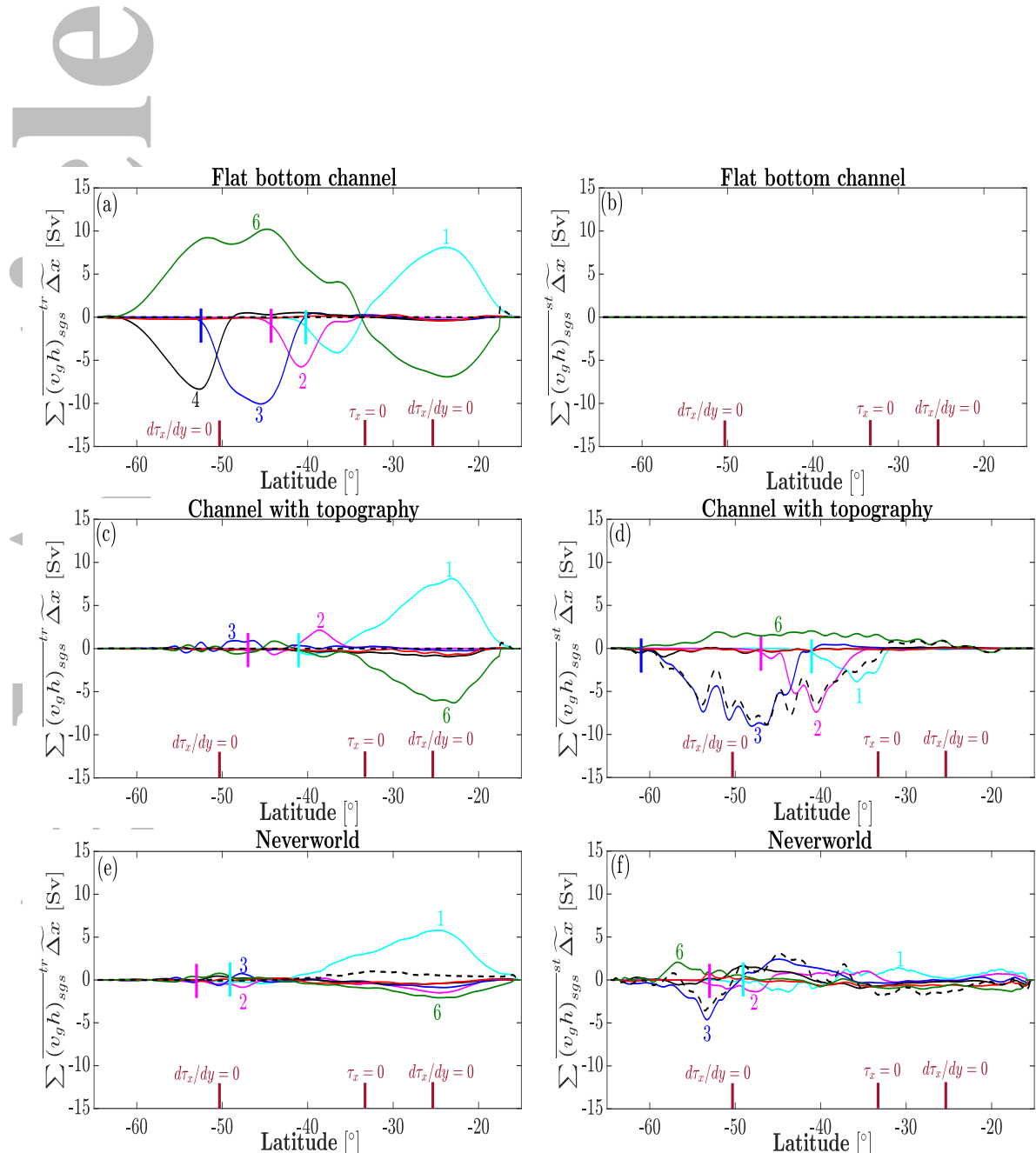
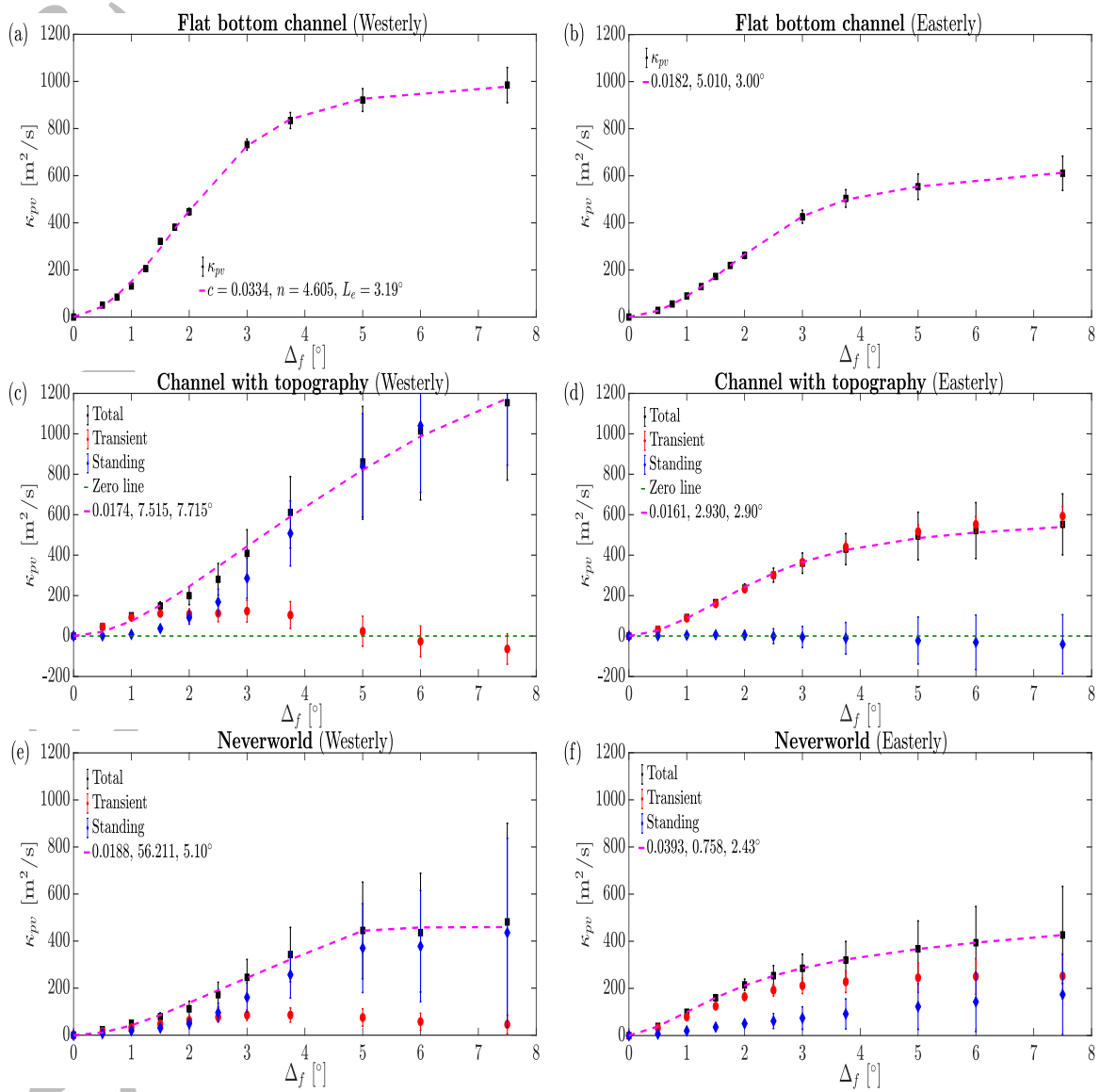


Figure 12.

Accepted Article

J
e
A
C
C



Accepted Article

Accepted Article

